

DOE/ER/41058-1

The University of Alabama in Huntsville

FINAL REPORT

Submitted to the U.S. Department of Energy,

PROGRAM ELEMENT: DE FG02-97ER41058

PROGRAM NAME:

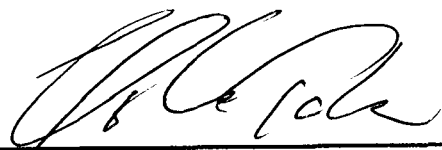
“Study of Isospin Correlation in High Energy Heavy Ion Interactions with the RHIC PHENIX”,

Principal Investigator:

Dr. Yoshiyuki Takahashi / Professor.

Department of Physics, The University of Alabama in Huntsville, Huntsville, AL35899,

TEL: (256) 824-2866; FAX: (256) 824-6873, E-mail: yoshi@cosmic.uah.edu



(Signature) Date: June 6, 2003

DOE Patent Clearance Granted

 9.16.03

Date

Mark P. Dvorscak
(630) 252-2393
E-mail: mark.dvorscak@ch.doe.gov
Office of Intellectual Property Law
DOE Chicago Operations Office

DISCLAIMER

This report was prepared as an account of work sponsored by an agency of the United States Government. Neither the United States Government nor any agency thereof, nor any of their employees, makes any warranty, express or implied, or assumes any legal liability or responsibility for the accuracy, completeness, or usefulness of any information, apparatus, product, or process disclosed, or represents that its use would not infringe privately owned rights. Reference herein to any specific commercial product, process, or service by trade name, trademark, manufacturer, or otherwise does not necessarily constitute or imply its endorsement, recommendation, or favoring by the United States Government or any agency thereof. The views and opinions of authors expressed herein do not necessarily state or reflect those of the United States Government or any agency thereof.

DISCLAIMER

Portions of this document may be illegible in electronic image products. Images are produced from the best available original document.

SUMMARY

This report describes the research work performed under the support of the DOE research grant E-FG02-97ER41048. The work is composed of three parts:

- (1) Visual analysis and quality control of the Micro Vertex Detector (MVD) of the PHENIX experiments carried out at Brookhaven National Laboratory.
- (2) Continuation of the data analysis of the EMU05/09/16 experiments for the study of the inclusive particle production spectra and multi-particle correlation. This experimental method using a magnetic emulsion spectrometer technique was new in the field of nuclear physics and heavy-ion studies.
- (3) Exploration of a new statistical means to study very high-multiplicity of nuclear-particle ensembles and its perspectives to apply to the higher energy experiments. This study particularly depicts, among many possible aspects of ensembles, multi-particle isospin correlation at high-energy densities that occurs in collisions of high energy heavy ions.

Throughout this grant period, 1997 – 2000, we emphasized the analysis and a study of multi-particle isospin correlation, using a statistical method which we call a canonical Fourier analysis. The results of this analysis in comparison with simulations were compiled in his dissertation by T. Shiina in April, 2003.

During the grant period, the UAH provided technical supports to the MVD Team at the Los Alamos National Laboratory for the RHIC PHENIX experiments. These work include:

- (i) visual inspection and quality assurance of kapton cables for the silicon micro-vertex detector;
- (ii) testing and installation of the Silicon strip detector and pad detector, and
- (iii) quality testing of a part of the front-end electronics.

Concerning our emphasis of the science part of this research that was proposed, we have studied the multi-particle correlation in a nuclear ensemble. It is a continuation of our studies since 1986 when high-energy heavy-ion experiments at Centre Européenne pour la Recherche Nucléaire (CERN), or European Organization for Nuclear Research, began. We have conducted the on-site experiments and measured at the home Institution,

the University of Alabama in Huntsville, particle tracks produced in the detector. Statistical data analysis and theoretical studies on the data were developed on the basis of these measured data. Throughout this grant period, 1997 – 2000, we developed an analysis for the study of multi-particle isospin correlation, using a statistical method which we call a canonical Fourier analysis. The results of this analysis in comparison with simulations were compiled in his dissertation by T. Shiina in April, 2003.

Students and Staffs supported:

GRA III Toshiyuki Shiina (on site at LLNL)

GRA I Jessica Gaskin

Post-graduate assistant: Chul Soon Yoon (on site at LLNL)

Undergraduate students: John Patti, Paul Whisant

Research Analyst II Bei Lei Dong

Degrees concurred to students

Toshiyuki Shiina, Ph. D, May, 2003

Jessica Gaskin, M.S., May, 2001.

List of technical tasks delivered to Los Alamos National Laboratory

1. Cable Inspection

a) software development and qualification and testing with it at UAH for the initial samples of the kapton cables. The results are used for bulk procurement at LLNL and were used for installation in the PHENIX experiments.

b) visual inspection of ~400 kapton cables (256 traces) under the microscope.

requirement - 100% continuity and no shorts.

c) electrical inspection of 250 kapton cables using LabView program.

requirement - 100% continuity and no shorts (Confirmation of 1-a).

d) visual inspection of 500 MCM output cables (50 traces) under the microscope

- requirement - 100% continuity and no shorts.
- d) electrical inspection of 500 MCM output cables.
 - requirement - 100% continuity and no shorts.
- e) estimate of dielectric breakdown voltage of MCM output cable.
 - requirement - ensure breakdown does not occur near Si bias voltage (~50V).
- f) electrical inspection of ZIF connectors for MCM output cables.
 - requirement - 100% continuity and no shorts and 100% mechanical fit.

2. Silicon strip detector and pad detector

- a) burn-in of ~50 silicon detectors using LabView program.
 - requirements - ensure total and guard ring leakage current of a silicon wafer is below specified value.
- b) measurement of individual channel leakage current.
 - requirement - ensure single channel leakage current of a silicon wafer is below specified value.
- c) measurement of depletion voltage of a silicon wafer.
 - requirement - ensure depletion voltage is well below bias voltage.
- d) measurement of silicon diode breakdown voltage.
 - requirement - ensure diode breakdown does not occur at the set bias voltage
- e) measurement of wafer thickness.
 - requirement - ensure wafer thickness meets the spec.
- f) measurement of coupling capacitance as a measure of wirebond quality.
 - requirement - ensure the wirebond quality is acceptable.
- g) measurement of inter-channel and signal channel to guard ring resistance.
 - requirement - identify shorted channels.
- h) measurement of bias line resistor value.
 - requirement - ensure resistor value of signal channel embedded in a wafer meets the spec.
- i) integration of various test results.
 - requirement - assign grade to a silicon wafer according to all the test results.
- j) keeping inventory list of silicon detectors.
 - requirements - keep a log book for grades and whereabouts.

3. Front End Electronics

- a) MCM quality testing.
requirements - ensure MCM returns reasonable ADC value to an output.
- b) silicon readout testing with infrared laser/LED.
requirements - ensure silicon detector responds to laser/LED.
- c) purchasing surface mount components of MCM.
requirements - identify part number and quality for various surface mount components.
- d) contacting surface mount and wirebond vendor.
requirements - define and describe problems and have them solved.

List of Publications

"Measurement of the Λ and $\bar{\Lambda}$ particles in Au + Au Collisions at $\sqrt{S_{NN}} = 130$ GeV"
(PHENIX Collaboration*)
Physical Review Letters v. 89, 092302 (2002)

"Flow Measurements via Two-particle Azimuthal Correlations in Au + Au Collisions at $\sqrt{S_{NN}} = 130$ GeV"
(PHENIX Collaboration*)
Accepted for publication in *Physical Review Letters*, [preprint nucl-ex/0204005](#)

"Event-by-event Fluctuations in Mean p_T and Mean e_T in $\sqrt{S_{NN}} = 130$ GeV Au+Au Collisions"
(PHENIX Collaboration*)
Physical Review C 66, 024901 (2002)

"Net Charge Fluctuations in Au+Au Interactions at $\sqrt{S_{NN}} = 130$ GeV"
(PHENIX Collaboration*)
Physical Review Letters v. 89, 082301 (2002)

"Measurement of Single Electrons and Implications for Charm Production in Au+Au Collisions at $\sqrt{S_{NN}} = 130$ GeV",
(PHENIX Collaboration*)
Physical Review Letters v. 88, 192303 (2002)

"Transverse-Mass dependence of Two-Pion Correlations for Au+Au collisions at $\sqrt{S_{NN}} = 130$ GeV"
(PHENIX Collaboration*)
Physical Review Letters v. 88, 192302 (2002)

"Centrality Dependence of $\pi^{+/-}$, $K^{+/-}$, p and \bar{p} Production from $\sqrt{S_{NN}} = 130$ GeV Au + Au Collisions at RHIC"
(PHENIX Collaboration*)
Physical Review Letters v. 88, 242301 (2002)

"Overview of PHENIX Results from the First RHIC Run"
[PHENIX Collaboration*]
Nuclear Physics A v.698 p.39c (2002)

"Suppression of Hadrons with Large Transverse Momentum in Central Au+Au Collisions at $\sqrt{S_{NN}} = 130$ GeV"
(PHENIX Collaboration*)
Physical Review Letters v. 88, 022301 (2002)

"First Results from RHIC-PHENIX"
(PHENIX Collaboration*)
Pramana, Journal of Physics, v.57, no.2-3, p.355 (2001)

"Measurement of the Midrapidity Transverse Energy Distribution from $\sqrt{S_{NN}} = 130$ GeV Au-Au Collisions at RHIC"
(PHENIX Collaboration*)
Physical Review Letters v. 87, 052301 (2001)

"Centrality Dependence of Charged Particle Multiplicity in Au-Au Collisions at $\sqrt{S_{NN}} = 130$ GeV"
(PHENIX Collaboration*)
Physical Review Letters v. 86, #16, 3500 (2001)

"Simulations of the performance of the MVD in PHENIX"
M. J. Bennett, J. Bernardin, J. Boissevain, C. Britton, J. Chang, D. Clark, R. Conway, R. Cunningham, M. Emery, N. Ericson, S. Y. Fung, S. Hahn, H. vanHecke, D. Jaffe, J. H. Kang, S. Y. Kim, Y. G. Kim, R. Lind, L. Marek, K. McCabe, T. Moore, J. H. Park, G. Richardson, S. S. Ryu, B. Schlei, R. Seto, T. Shiina, J. SimonGillo, M. Simpson, G. Smith, J. P. Sullivan, Y. Takahashi, A. Wintenber, and G. Xu
IEEE Transactions on Nuclear Science v. 46, #6/pt.2, 2022 (1999)

"The PHENIX Multiplicity and Vertex Detector"
M. J. Bennett, M. Bobrek, J. G. Boissevain, C. L. Britton, J. Chang, R. Conway, R. Cunningham, M. S. Emery, M. N. Ericson, S. -Y. Fung, S. Hahn, H. W. van Hecke, D. Jaffe, J. H. Kang, S. Y. Kim, Y. G. Kim, L. J. Marek, J. A. Moore, J. H. Park, G. Richardson, S. S. Ryu, B. R. Schlei, T. Shiina, J. Simon-Gillo, G. Smith, C. Y. Soon, J. P. Sullivan, Y. Takahashi, and G. Xu
Nuclear Physics A v.661, pp.661 (1999)

"Interpreting Anomalous Electron Pairs As New Particle Decays"
K. Asakimori, T. H. Burnett, M. L. Cherry, K. Chevli, M. J. Christl, S. Dake, J. H. Derrickson, W. F. Fountain, M. Fuki, J. C. Gregory, T. Hayashi, J. Iwai, A. Iyono, J. Johnson, M. Kobayashi, J. J. Lord, O. Miyamura, K. H. Moon, H. Oda, T. Ogata, E. D. Olson, T. A. Parnell, F. E. Roberts, T. Shiina, S. C.

Strausz, T. Sugitate, Y. Takahashi, T. Tominaga, J. W. Watts, J. P. Wefel, B. Wilczynska, H. Wilczynski, R. J. Wilkes, W. Wolter, H. Yokomi, and E. Zager
Journal of Physics G-Nuclear and Particle Physics v. 25, #12, L133 (1999)

“The PHENIX experiment at RHIC”
[PHENIX Collaboration*]
Nuclear Physics A v. A638, no.1-2, p.565c (1998)

“Cosmic-ray Proton and Helium Spectra: Results from the JACEE Experiment”
K. Asakimori, T. H. Burnett, M. L. Cherry, K. Chebli, M. J. Christ, S. Dake, J. H. Derrickson, W. F. Fountain, M. Fuki, J. C. Gregory, T. Hayashi, R. Holynski, J. Iwai, A. Iyono, J. Johnson, M. Kobayashi, J. Lord, O. Miyamura, K. H. Moon, B. S. Nilsen, H. Oda, T. Ogata, E. D. Olson, T. A. Parnell, F. E. Roberts, K. Sengupta, T. Shiina, S. C. Strausz, T. Sugitate, Y. Takahashi, T. Tominaga, J. W. Watts, J. P. Wefel, B. Wilczynska, H. Wilczynski, R. J. Wilkes, W. Wolter, H. Yokomi, and E. Zager
Astrophysical Journal v. 502, #1/pt.1, 278 (1998)

“Elemental Abundance of High Energy Cosmic Rays”
Y. Takahashi, K. Asakimori, T. H. Burnett, M. L. Cherry, K. Chebli, M. J. Christl, S. Dake, J.H. Derrickson, W. F. Fountain, M. Fuki, J. C. Gregory, R. Holynski, J. Iwai, A. Iyono, M. V. Jones, A. Jurak, M. Kobayashi, J. J. Lord, O. Miyamura, H. Oda, T. Ogata, E. D. Olson, T. A. Parnell, F. E. Roberts, T. Shiina, S. C. Strausz, T. Tominaga, S. Toyoda, J. W. Watts, J. P. Wefel, B. Wilczynka, H. Wilczynski, R. J. Wilkes, W. Wolter, B. Wosiek, H. Yokomi, E. L. Zager
Nuclear Physics B v.(S60B), pp. 83(1998)

“Cosmic Ray H and He Spectra from 2 to 800 TeV/nucleon from the JACEE Experiments”
B. S. Nilsen, K. Asakimori, T. H. Burnett, M. L. Cherry, K. Chebli, M. J. Christl, S. Dake, J. H. Derrickson, W. F. Fountain, M. Fuki, J. C. Gregory, T. Hayashi, A. Iyono, J. Iwai, J. Johnson, M. Kobayashi, J. Lord, O. Miyamura, K. H. Moon, H. Oda, T. Ogata, E. D. Olson, T. A. Parnell, F. E. Roberts, K. Sengupta, T. Shiina, S. C. Strausz, T. Sugitate, Y. Takahashi, T. Tominaga, J. W. Watts, J. P. Wefel, B. Wilczynska, H. Wilczynski, R. J. Wilkes, W. Wolter, H. Yokomi, E. Zager
AIP Conference Proceedings; no.412, p.1031 (1997)

Presentations

Toshiyuki Shiina, “The PHENIX Multiplicity and Vertex Detector,” American Physical Society Centennial Meeting, March 20-26, 1999, Atlanta, GA, Session VB12 - RHIC Instrumentation and Beams. Contributed oral presentation.

Technical Notes Posted on World Wide Web

Toshiyuki Shiina, “Gluing Procedure for MCM to MCM Output Cable”
http://p25ext.lanl.gov/phenix/mvd/construction/procedures/mcm_to_opc_glue_procedure.html 1999

Toshiyuki Shiina, “Gluing Procedure for Si Strip Detector + Katon Cable Assembly to MCM + MCM Output Cable Assembly”

http://p25ext.lanl.gov/phenix/mvd/construction/procedures/sikap_to_mcmopc_glue_procedure.html 1999

Toshiyuki Shiina, "Kapton Cable Quality Assurance Procedure"
<http://p25ext.lanl.gov/phenix/mvd/construction/procedures/kaptoncableQA.html>
1999

Mike Bennett, David Jaffe, and Toshiyuki Shiina, "Microstrip Detector to Kapton Cable Wirebond Quality Assurance Procedure"
<http://p25ext.lanl.gov/phenix/mvd/construction/procedures/wirebondqa2.html>

Toshiyuki Shiina, "MCM Output Cable Quality Assurance Procedure"
<http://p25ext.lanl.gov/phenix/mvd/notes/1999/PHENIX-MVD-99-4/mcmqad2.html>
1999 PHENIX-MVD-99-4, PHENIX Note 372

LANL Unclassified Technical Note
Toshiyuki Shiina, John Sullivan, Mohini Rawool-Sullivan, "Silicon Pixel Detector Testing" (to be published) 2002

Full Report of the Isospin Correlation Study

1. INTRODUCTION

Earlier, we carried out the first nucleus-nucleus interaction studies in cosmic ray experiments known as the Japanese-American-Cooperative-Emulsion-Experiments (JACEE) [1]. When high-energy heavy-ion beams (60 and 200 GeV/nucleon) became available at CERN SPS in the fall of 1986, the emulsion experiment EMU05 was designed and carried out [2]. EMU05 measures multiplicity, angular distributions, momenta, and charge-signs of the secondary charged particles emerging from collisions with lead ions in an emulsion chamber placed in a uniform 1.8 Tesla magnetic field. This new detector enabled a comprehensive experimental study of high density nuclear matter and the mechanism of multi-particle production in detail. In the early stages of analysis in 1986 we noticed an apparent charge-sign “clustering” in the angular distribution of charged particles of one of the highest multiplicity events. Figure 1.1 shows the target diagram of one such event (200GeV/nucleon S + Pb, event #4750. Figure 1.1 shows a portion of the event #4750 (EMU-05) with pseudorapidities ranging from 0.7 to 2.4 where the clustering is most apparent. Solid (+) and dashed (-) lines are drawn to subjectively show apparent clusters of like-sign particles, and it suggests that the negative clusters and positive clusters appeared side by side periodically. EMU05 first examined the statistical significance of such charge-sign clusters by an objective analysis called the “run-test” and then examined the degree of clustering vs. random coincidence by the “conjugate test” (G-test) [3]. During the present grant period we carried out a third objective cluster analysis – canonical Fourier analysis – by examining the statistical significance of the periodicity of the negative and positive charged clusters as well as the degree of the clustering using a method previously applied in astrophysics, Lomb’s periodogram [4]. This new analysis method was applied to 42 high-energy central collision events from EMU05, EMU09, and EMU16 heavy-ion experiments carried out at CERN, and the signatures a possible formation of quark-gluon plasma (QGP) and disoriented chiral condensate (DCC) were investigated. Our results showed little evidence for them.

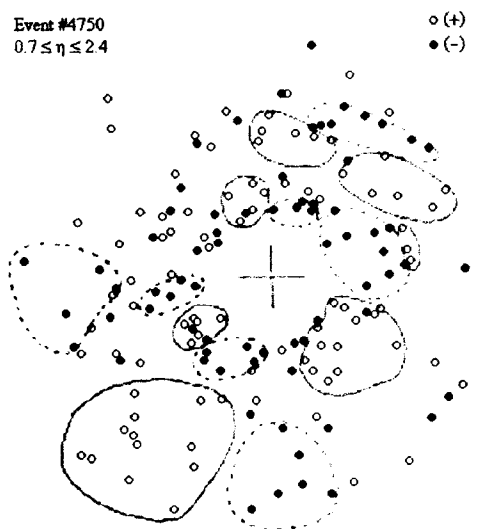


Figure 1.1 Target diagram of $^{32}\text{S} + \text{Pb} \rightarrow 535$ event (EMU05: event #4750) [2][3].

1.1 Estimate of Source Size

The method to estimate the space-time size of a thermal pion source (plasma ball) has been well established [33][34]. The correlation of two identical particles, such as π^- and π^- , can be calculated by the Hanbury-Brown and Twiss (HBT) effect assuming that those particles can be treated as free particles. F. B. Yano and E. Koonin state that the plane wave approximation is very well applicable because the strong interaction and the Coulomb interaction between the particles are negligible after the particles leave the source [35]. Figure 2.15 shows a diagram of two identical pions detected at two detectors.

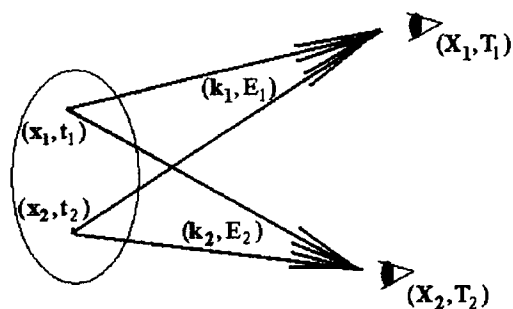


Figure 1.2 Thermal pion source and detectors. – A pion of momentum \mathbf{k}_1 and energy E_1 is detected at detector 1 at time T_1 , and an identical pion of momentum \mathbf{k}_2 and energy E_2 is detected at detector 2 at time T_2 .

Since it is impossible to distinguish the origins of two identical pions, we must add two amplitudes as required by Bose statistics [33].

When two identical particles are emitted from two independent points \mathbf{x}_1 and \mathbf{x}_2 in the same source at independent time t_1 and t_2 , (\mathbf{x}_1, t_1) and (\mathbf{x}_2, t_2) respectively, and detected at (\mathbf{X}_1, T_1) and (\mathbf{X}_2, T_2) having the momentum and the energy of (\mathbf{k}_1, E_1) and (\mathbf{k}_2, E_2) , the correlation function C_2 is given by

$$C_2 = \int |\Psi_{12}(\mathbf{X}_1, T_1; \mathbf{X}_2, T_2)|^2 \rho_s(\mathbf{x}_1, t_1) \rho_s(\mathbf{x}_2, t_2) d\mathbf{x}_1 d\mathbf{x}_2 dt_1 dt_2 ,$$

where $\Psi_{12}(\mathbf{X}_1, T_1; \mathbf{X}_2, T_2)$ is the probability amplitude for a pair of identical pions created at location 1 and 2 in the same source being detected at detector 1 and 2 and given by

$$\Psi_{12}(\mathbf{X}_1, T_1; \mathbf{X}_2, T_2) = \frac{1}{\sqrt{2}} \begin{vmatrix} \exp[i\mathbf{k}_1(\mathbf{X}_1 - \mathbf{x}_1)/\hbar - iE_1(T_1 - t_1)/\hbar] \cdot \\ \exp[i\mathbf{k}_2(\mathbf{X}_2 - \mathbf{x}_2)/\hbar - iE_2(T_2 - t_2)/\hbar] \\ + \exp[i\mathbf{k}_1(\mathbf{X}_1 - \mathbf{x}_2)/\hbar - iE_1(T_1 - t_2)/\hbar] \cdot \\ \exp[i\mathbf{k}_2(\mathbf{X}_2 - \mathbf{x}_1)/\hbar - iE_2(T_2 - t_1)/\hbar] \end{vmatrix}$$

and $\rho_s(\mathbf{x}, t)$ is the space-time structure of the source, which can be assumed to be Gaussian distribution function expressed as

$$\rho_s(\mathbf{x}, t) = \frac{1}{\pi^2 R_s^3 \tau_s} \exp(-\mathbf{x}^2 / R_s^2) \exp(-t^2 / \tau_s^2),$$

where τ_s is the lifetime and R_s is the radius of the thermal pion source. After carrying out the integral, C_2 becomes

$$C_2 = 1 + \lambda_C \exp[-|\mathbf{k}_1 - \mathbf{k}_2|^2 R_s^2 / 2\hbar^2 - (E_1 - E_2)^2 \tau_s^2 / 2\hbar^2],$$

where λ_C is a parameter introduced to indicate the interference strength. In the ideal case of a chaotic source, $\lambda_C = 1$.

The definition of the correlation function is the ratio of the probability of finding two particles having momenta \mathbf{k}_1 and \mathbf{k}_2 versus the probability of finding one particle having the momentum \mathbf{k}_1 and the other with \mathbf{k}_2 , which suggests

$$C_2 = \frac{dN}{d(|\mathbf{k}_1 - \mathbf{k}_2|)} / \frac{dN}{d(|\mathbf{k}_1|)} \frac{dN}{d(|\mathbf{k}_2|)} .$$

Thus the parameter λ_C and the source radius R_s can be obtained by fitting the calculated C_2 function to the momentum spectra (neglecting the time dependence). The acceptance of EMU05 (almost 4π in the CM frame) is large enough to determine the source radius R_s . Y. Takahashi, et al., applied this HBT method to 16 EMU05 events obtained earlier and reported $R_s = 4.2 \pm 2.2$ fm, with the interference strength, $\lambda_C = 0.37 \pm 0.19$ for π^- pairs in the pseudorapidity region, $2 < y_R < 4$ (See Figure 1.3) [2].

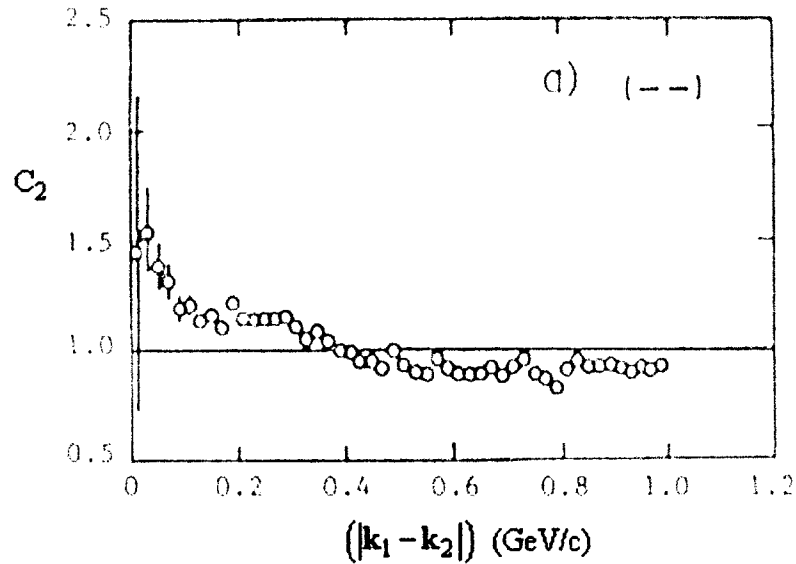


Figure 1.3 C_2 function for π^- pairs (16 EMU05 events) [2].

The initial radius of the projectile-target interaction region for sulfur + lead collision should be about the radius of the projectile sulfur ($R_p \approx 1.5$ fm). The large source size reported by EMU05 collaboration suggests interference of pions in a gas of hadrons expanding from an initially small hot interaction region.

§ 2. Theoretical Prediction of Disoriented Chiral Condensate

In order to understand theoretically predicted DCC formation, we'll first review the basic property of isospin rotation and chiral transformation in the following sections.

2.1 Counterclockwise rotation of wave function ψ by infinitesimal angle $\delta\theta_r$

Let us begin by discussing operation of the angular momentum operator L on a wave function $\Psi(x, y, z, t)$ in the regular space. We, then, generalize the concept and make application to the rotation in the isospin space to discuss chirality and chirally symmetric QCD vacuum [39][11].

Suppose we rotate a wave function $\Psi(x, y, z, t)$ by an infinitesimal angle $\delta\theta_r$ about the z axis in the counterclockwise direction. The wave function $\Psi(x, y, z, t)$ then, will be transformed into $\Psi'(x, y, z, t)$. But under the assumption of rotational symmetry of space, the operation is equivalent to a rotation of the coordinate system clockwise by $\delta\theta_r$. (Rotational symmetry of space yields conservation of angular momentum by Neother's theorem.) Thus

$$\text{Rotation}(\Psi \rightarrow \Psi'): \Psi'(x, y, z, t) = \Psi(x', y', z', t),$$

where

$$\begin{pmatrix} x' \\ y' \\ z' \end{pmatrix} = \begin{pmatrix} \cos(-\delta\theta_r) & \sin(-\delta\theta_r) & 0 \\ -\sin(-\delta\theta_r) & \cos(-\delta\theta_r) & 0 \\ 0 & 0 & 1 \end{pmatrix} \begin{pmatrix} x \\ y \\ z \end{pmatrix} \approx \begin{pmatrix} x - y\delta\theta_r \\ y + x\delta\theta_r \\ z \end{pmatrix}.$$

So

$$\Psi'(x, y, z, t) = \Psi(x - y\delta\theta_r, y + x\delta\theta_r, z, t).$$

Since $\delta\theta_r$ is infinitesimal, we can apply a Taylor series expansion and keep only 0th and 1st order terms in $\delta\theta_r$.

$$\begin{aligned} & \Psi'(x, y, z, t) \\ &= \Psi(x, y, z, t) + (-y\delta\theta_r) \frac{\partial \Psi(x, y, z, t)}{\partial x} + (x\delta\theta_r) \frac{\partial \Psi(x, y, z, t)}{\partial y} + O((\delta\theta_r)^2) \\ &\approx \left[1 + \delta\theta_r \left(x \frac{\partial}{\partial y} - y \frac{\partial}{\partial x} \right) \right] \Psi(x, y, z, t) \\ &= \left(1 + i \frac{\delta\theta_r L_z}{\hbar} \right) \Psi(x, y, z, t) \end{aligned}$$

by definition of $L_z \left(= -i\hbar \left(x \frac{\partial}{\partial y} - y \frac{\partial}{\partial x} \right) \right)$. Here the angular momentum operator

$\mathbf{L} (= (L_x, L_y, L_z))$ satisfies the commutation relation:

$$[L_x, L_y] = i\hbar L_z, [L_y, L_z] = i\hbar L_x, \text{ and } [L_z, L_x] = i\hbar L_y.$$

2.3. Counterclockwise rotation of wave function ψ by finite angle θ_r

Next we consider rotation of a wave function by a finite angle θ_r about the z axis. The finite angle rotation can be achieved by the successive application of small angle rotations by θ_r / ℓ ($\ell \gg 1$) ℓ times and letting $\ell \rightarrow \infty$. That is,

$$\begin{aligned} \Psi'(x, y, z, t) &= \lim_{\ell \rightarrow \infty} \left(1 + i \frac{\theta_r L_z}{\ell \hbar} \right)^\ell \Psi(x, y, z, t) \\ &= \exp \left(\frac{i\theta_r L_z}{\hbar} \right) \Psi(x, y, z, t) \end{aligned}$$

In general using the angular momentum operator \mathbf{L} , the rotation operator can be expressed as $\exp\left(\frac{i\boldsymbol{\theta}_r \cdot \mathbf{L}}{\hbar}\right)$, where the vector $\boldsymbol{\theta}_r$ represents the direction of the rotation axis and the magnitude θ_r ($= |\boldsymbol{\theta}_r|$). The sign of θ_r represents the direction of rotation, -: clockwise rotation and +: counterclockwise rotation.

2.4 Application of the rotation operator to the spin space

We generalize the definition of the rotation operator in the regular space and define the rotation operator in the spin space as follows:

$$\exp\left(\frac{i\boldsymbol{\theta}_s \cdot \mathbf{J}}{\hbar}\right),$$

and apply 2π rotation around the z axis. That is,

$$\exp\left(\frac{i2\pi J_z}{\hbar}\right) = \exp(i\pi \sigma_{Pz}) = \cos \pi + i\sigma_{Pz} \sin \pi = -1.$$

Thus, in general, spin rotation about the third axis by 2π changes the sign of the wave function of spin $\hbar/2$ particles.

2.5. Generalization of rotation operator to isospin space

Isospin is a quantum number assigned to a particle which is conserved in strong interactions. For example, neutrons and protons interact similarly under strong interaction. One can understand them as different charge states of the same particle, the nucleon with isospin $I = 1/2$. We assign the third component of the isospin $I_3 = 1/2$ to a proton and $I_3 = -1/2$ to a neutron. This formal description of isospin is completely analogous to that of a particle with ordinary spin $\hbar/2$. We further generalize the concept of rotation and angular momentum to isospin space and describe isospin rotation by $|\theta_I|$ as

$$\text{Isospin rotation operator: } \exp(i\theta_I \cdot \mathbf{I}),$$

where $\mathbf{I} = \frac{1}{2} \boldsymbol{\tau}$ and $\boldsymbol{\tau} = (\tau_1, \tau_2, \tau_3)$. $\boldsymbol{\tau}$ is a three component vector and each component takes the same form as Pauli matrices.

A similar notation as the spin $1/2\hbar$ case can be used for isospin $1/2$ particles. Then, for example, a proton is represented by isospin up state $\begin{pmatrix} 1 \\ 0 \end{pmatrix}$, and a neutron is represented by isospin down state $\begin{pmatrix} 0 \\ 1 \end{pmatrix}$. The neutron state can be generated by applying an isospin rotation operator to the proton state. The fact that both a proton and a neutron feel strong force and their mass is very close ($\sim 940 \text{ MeV}/c^2$) implies that $[\mathbf{I} \cdot \mathbf{H}] = 0$ holds approximately (conservation of isospin in strong interactions), where \mathbf{H} is a Hamiltonian of the system. The corresponding symmetry is called SU(2) symmetry.

The QCD vacuum is understood to be a field of condensation of the massless quark and antiquark pair, which is isotropic and uniform, and a quark carries a spin $1/2\hbar$.

2.6 QCD Lagrangian and Chiral Symmetry

For a single quark field, free quark QCD Lagrangian is given as

$$L = \bar{q}[i\gamma^\mu \partial_\mu - m_q]q,$$

where q is a solution of Dirac equation and $\bar{q} = q^\dagger \gamma^0$ (adjoint) [40].

This Lagrangian is invariant under chiral transformation of the quark field through an arbitrary angle θ :

$$q \rightarrow e^{i\gamma^5 \theta} q \text{ and } \bar{q} \rightarrow \bar{q} e^{i\gamma^5 \theta},$$

when we consider the mass of a quark to be zero as discussed before. We consider the system of two lightest quarks - u and d quarks – in SU(2) symmetry where current quark masses are negligible in the following sections. The generalization of chiral transformation for two quark flavors is given as

$$\bar{q} \rightarrow \exp[i\gamma^5 \boldsymbol{\tau} \cdot \boldsymbol{\theta}/2] \bar{q} \text{ and } q \rightarrow q \exp[i\gamma^5 \boldsymbol{\tau} \cdot \boldsymbol{\theta}/2],$$

where the angle $\boldsymbol{\theta}$ has three independent components representing the angles of rotation in isospin space.

This chiral transformation (rotation in isospin space) leaves the Lagrangian invariant in the massless limit of u and d quarks. Therefore chiral symmetry is an approximately valid symmetry because of small but finite u and d quark masses. Approximate chiral symmetry in QCD Lagrangian implies that if we observe a particle, we should observe a chirally transformed particle as well. Since chiral transformation changes the parity of a particle, for example, if we observe a pion, we should observe a positive parity pion (scalar pion) as well [18]. However, no positive parity pions exist. There is obviously a puzzle. The linear sigma model, which was first introduced by M. Gell-man and M. Levy in 1960, offers the answer to this puzzle [41][42].

2.7 Disoriented Chiral Condensate (DCC)

Lattice QCD calculation suggests that the expectation value of quark condensate reduces to zero at critical temperature as we reviewed [19]. This means the expectation value of sigma field vanishes. The implication of this is that a vacuum which is in the Goldstone mode transitions into the Wigner mode when two energetic heavy ions collide and the temperature rises higher than the critical temperature in some region of space and time. Hence, spontaneously broken chiral symmetry becomes restored (chiral symmetry restoration) [44] – [60]. The system then sits in the middle of the potential. As the surrounding system starts to cool down, the region of the hot vacuum may find itself sitting on top of a potential hill because as the temperature decreases, the quark condensate expectation value increases (Figure 2.1). This state is highly unstable. This

system may relax into a misaligned vacuum with a non-vanishing expectation value of the pion field – Disoriented Chiral Condensate (DCC) (Figure 2.2).

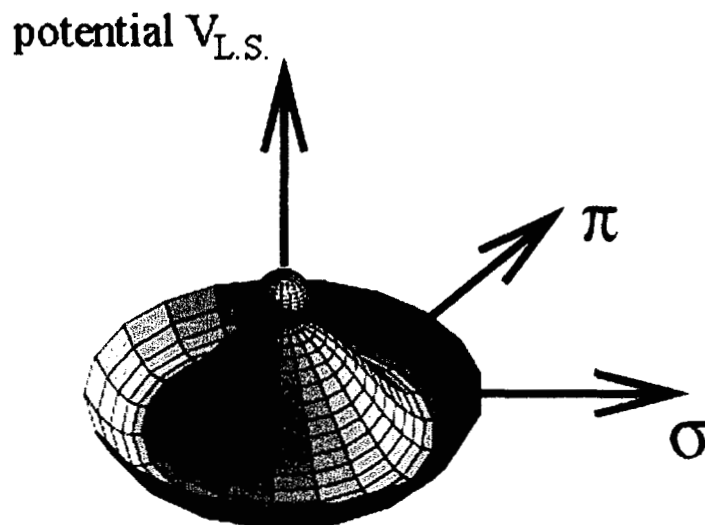


Figure 2.1 Chiral symmetry restoration [43].

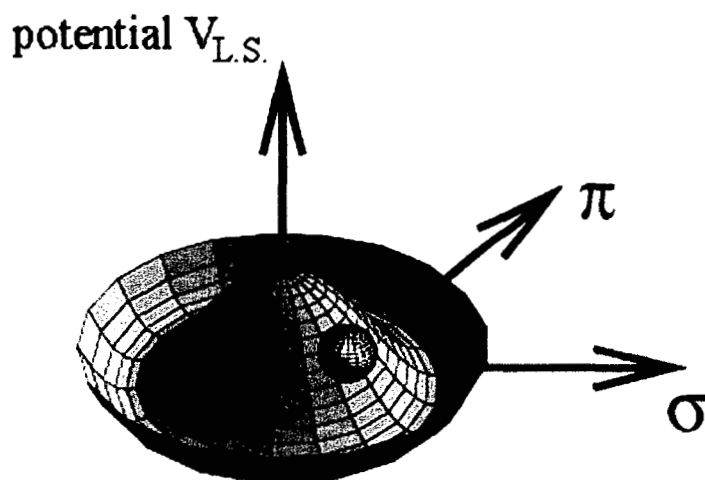


Figure 2.2 Disoriented chiral condensate [43].

The idea of formation of DCC and its relaxation to a normal vacuum, where chiral symmetry is spontaneously broken, in high energy heavy ion collisions has been suggested by many theorists [44] – [60]. In the following section observable consequences of DCC predicted by theory will be reviewed.

2.8 Baked Alaska Scenario – Bjorken Picture

In an attempt to explain peculiar cosmic ray events [1][61], J. D. Bjorken, et al., suggested that, in a high energy heavy ion collision, an expanding hot thin shell of collision debris may allow an isolated cold interior to exist for the proper time of a few fermi [62]. This bubble of isolated region surrounded by a hot shell is called Baked Alaska, and in the interior vacuum chiral orientation may be different (DCC) from that of the exterior region where the vacuum orientation is in the σ direction. As the expanding shell hadronizes, the DCC should radiate coherent pions of the same kind as the disoriented vacuum initially points in the four-dimensional chiral space. If the vacuum initially points in the direction of a neutral pion field, the radiated pions would be all neutral, and if the vacuum points in the direction perpendicular to the neutral pion, the DCC should radiate all charged pions. Since the initial orientation of the vacuum of DCC varies event by event, one can expect large event by event fluctuations of the neutral pion ratio. This could explain so-called Centauro, where the neutral pions ratio is unusually small [61], or Anti-Centauro events. An Anti-Centauro event was reported by JACEE collaboration [1]. The JACEE event (Figure 2.3) shows not only the abundance of gamma particles in large part of pseudorapidity-azimuth space ($\Delta\eta \cong 2$, $\Delta\phi \cong \pi$) but also the absence of charged particles in the same region. EMU05, EMU09, or EMU16 does not include neutral particle tracking capability. However such absence of charged particle from one apparently large $\eta-\phi$ space should be noticed as large fluctuations in pseudorapidity distributions immediately.

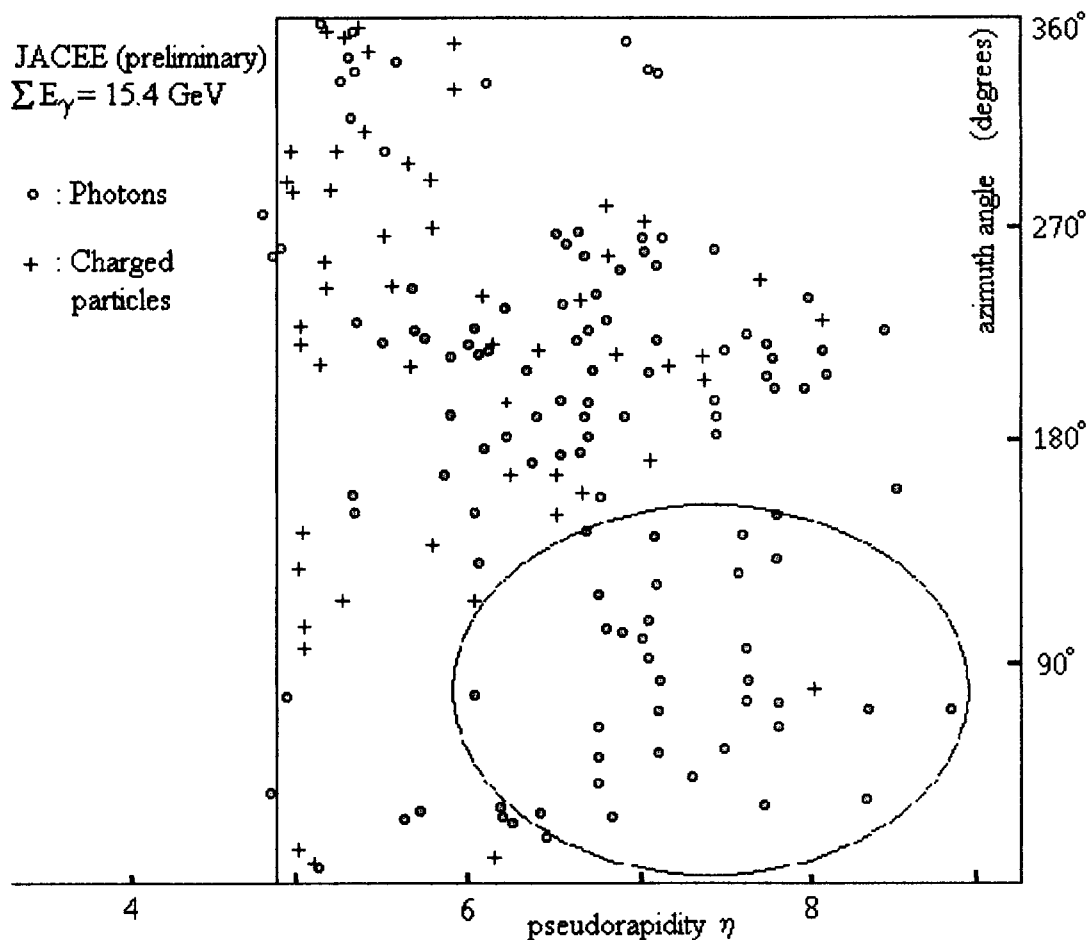


Figure 2.3 JACEE event showing the leading particles at $\eta > 5$ [1].

2.9 Quench Scenario – Rajagopal Wilczek Picture

In a region of possible quark gluon plasma left behind two high energy incident nuclei (Figure 2.13), the baryon number is small and the initial temperature is well above the critical temperature of chiral symmetry restoration. K. Rajagopal and F. Wilczek suggest that this hot plasma cools rapidly (quench) as it expands. They apply the linear sigma model to the system with an explicit symmetry breaking term using zero temperature equation of motion with $T > T_C$ initial condition in order to simulate the quench condition [45]. It was found that the state of the DCC would oscillate about the sigma direction relaxing to the ground state by coherent pion emission. This oscillation may create clusters of coherent pions with an alternating pion isospin state in some rapidity–azimuth space.

2.10 Chiral U(1) Scenario – Minakata Müller Asakawa Picture

H. Minakata and B. Müller argue that, in highly energetic heavy ion collisions, it is natural to consider the affect of a strong electromagnetic field on the possible DCC formation and its decay because a strong electromagnetic field breaks isospin symmetry and chiral U(1) anomaly (Adler-Bell-Jackiw anomaly) [63][64] should give an extra term in the sigma model Lagrangian for interactions between neutral pions and strong electromagnetic field [65]. They further predict that Anti-Centauro events should occur more often than Centauro events due to the interaction of neutral pions given rise to from the U(1) chiral anomaly. M. Asakawa, et al. [66] assume rapid quenching from the chirally symmetric phase to the conditions below the QCD critical temperature T_C and argue that semi-central events would enhance the effect of the Adler-Bell-Jackiw anomaly term introduced by H. Minakata and B. Müller. Their numerical calculations show an enhancement of neutral pion production in the form of the ratio of neutral pion multiplicity vs. total pion multiplicity. The Adler-Bell-Jackiw effect is clearly seen as the neutral pion enhancement at $\phi = 90$ and $\phi = 270$ degrees (Figure 2.4) when the DCC domain size is comparable to the value reported by EMU05 [2] (4.2 ± 2.2 fm) [66].

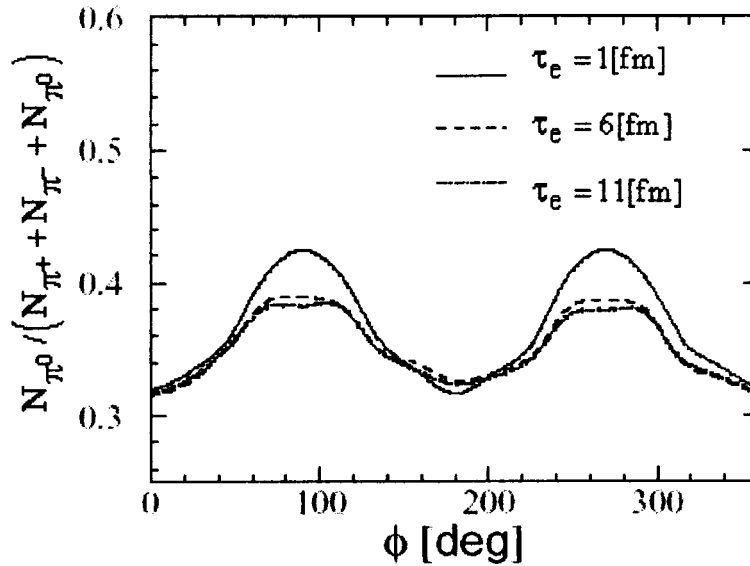


Figure 2.4 Azimuth angle dependence of the neutral pion ratio for the domain size of 5 fm [66]. – τ_e is the evolution time from the impact. ϕ is the azimuth angle normal to the incident beam axis.

High energy heavy ion collision is a highly complex phenomenon. All the conditions that were assumed in theories may or may not be satisfied. However, encouraged by Asakawa's numerical demonstrations, we try to find an answer, in the quenching scenario of the DCC, to the charge (or isospin) clustering that we observed in the EMU05 experiment in the quenching scenario of the DCC.

2.11 Previous EMU05 Cluster Analysis

The previous EMU05 analysis showed apparent clustering of charged particles in a few events [2][3]. The "run test" and the "conjugate test"(G-test) were applied to examine the degree of clustering vs. random coincidence. The run (r_r) is defined by the total number of sign-changes in a line of charges aligned in the order of azimuth angle (or rapidity) in one segment of rapidity-azimuth angle space. The normalized run (x_N), defined by $x_N = (r_r - \langle r_r \rangle) / \text{variance}$, should follow the normal distribution (0, 1) if charge-signs are randomly distributed while clusters should show negative x_N excess. Figure 2.5 shows the result of a normalized run test performed on event #4750 whose target diagram is shown in Figure 1.1. The x_N distribution for this event shows small deviation from the normal distribution toward negative direction.

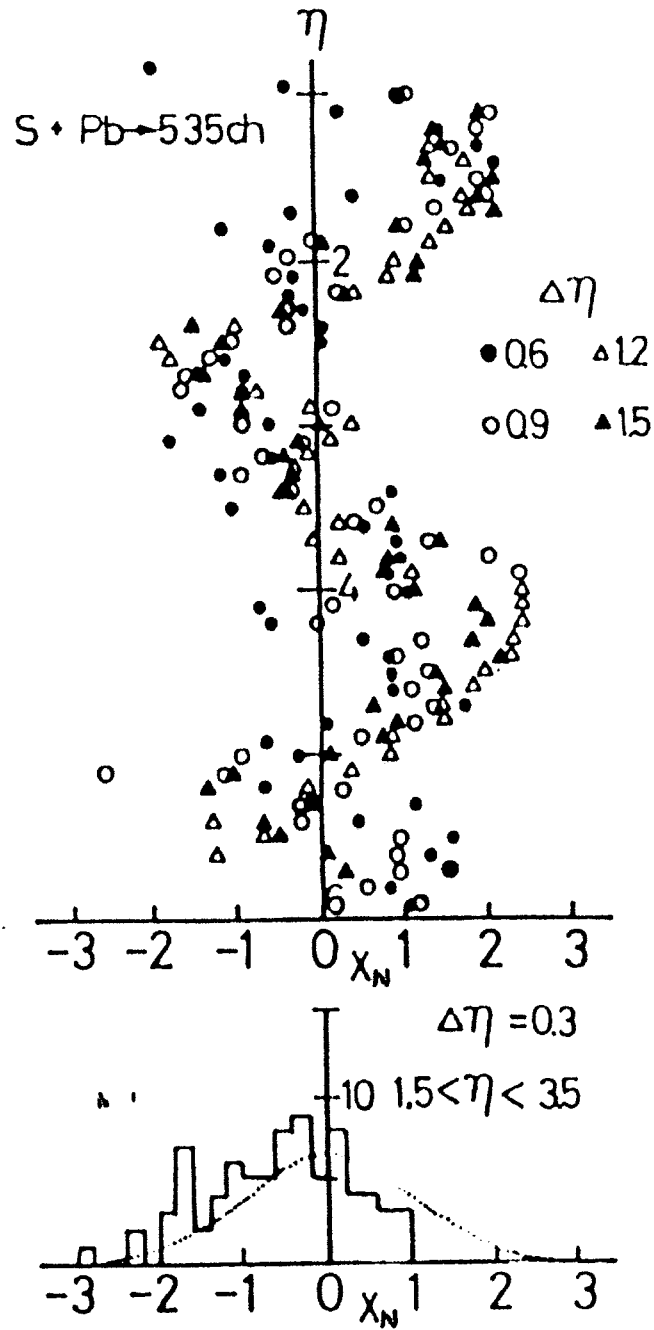


Figure 2.5 “Normalized run” test result (Event #4750 EMU-05) [2][3].

The G-test measures the degree of clustering by the quantity $G_i(\max)$ for the i -th particle. $G_i(\max)$ is defined as the maximum value of

$$G_{ij}(R_{\eta\phi}(i,j)) \\ \equiv \sum_{\kappa} \sum_{\lambda} C_{\kappa} \times C_{\lambda} \left(\kappa \neq \lambda \text{ and } R_{\eta\phi}(i,\kappa), R_{\eta\phi}(i,\lambda) \leq R_{\eta\phi}(i,j) \right),$$

where $R_{\eta\phi}(i,j)$ is a distance in pseudorapidity – azimuth angle space between the i -th particle and j -th particles defined by

$$R_{\eta\phi}(i,j) \equiv \cosh(\eta_j - \eta_i) - \cos(\phi_j - \phi_i),$$

when the index j is varied from 1 to the total multiplicity of the event ($j \neq i$). C_{κ} is the charge sign of κ -th particle. ($C_{\kappa} = +1$ for if κ -th particle is positively charged, and $C_{\kappa} = -1$ if κ -th particle is negatively charged.)

For example, if 7 particles contained in the radius of $R_{\eta\phi}(i,j)$ from i -th particle are all negatively charged, $G_i(\max)$ would be ${}_7C_2 (= 21)$. G-test examines statistical significance of clustering by comparing the distribution of $G_i(\max)$ value against Monte Carlo simulation. Figure 2.24 shows the $G_i(\max)$ value of all particles of the event #4750. The size of symbols (square for positive and cross for negative) is proportional to $G_i(\max)$ in the figure. Symbols shown in the upper right corner represent particles with a G value larger than 20. Despite a few appealingly large G values, the distribution was not significantly different from that of Monte Carlo simulation (Figure 2.7).

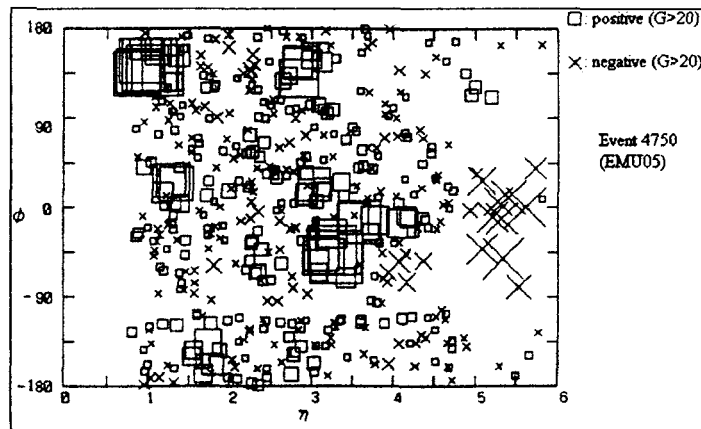


Figure 2.6 “G plot” [2]. – Size of the symbols is proportional to G value.

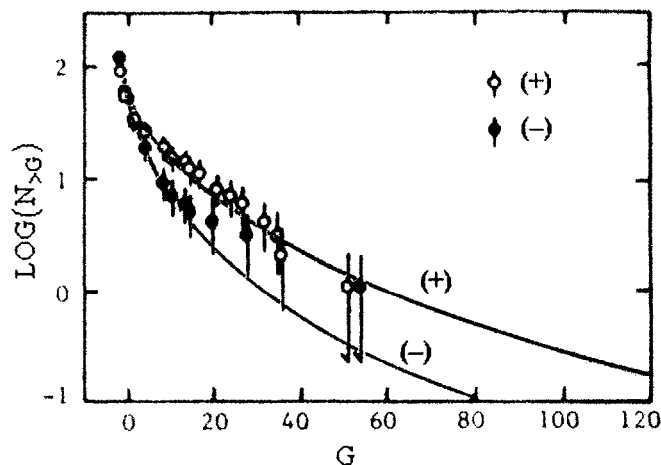


Figure 2.7 G value distribution for the event #4750 compared with Monte Carlo simulation [2]. — Ordinate is the number of particles whose G value is larger than abscissa. Solid lines represent G value distribution of a Monte Carlo simulation.

The run-test indicated random coincidence dominance over any possible signals of clusters. The G-test, on the other hand, showed negative-charge clusters in the projectile region for some S + Pb events. Although both the run-test and the G-test are powerful for an observer to recognize the existence of clusters, a cyclic combinatory degree of freedom is not sufficiently incorporated. There might be various hidden degrees of freedom in complicated multi-particle combinations. Quantitative means to assess the degree of correlation of opposite sign clusters side-by-side do not exist in these methods. We introduce a canonical Fourier analysis to improve this point of the multi-particle, multi-species statistical examination.

3. EXPERIMENTAL APPARATUS, MEASUREMENT OF CHARGED PARTICLES, AND INCLUSIVE DATA

We describe an experimental method of data acquisition along with an inclusive data set for EMU05, EMU09, and EMU16 experiments in this chapter.

§3.1 CERN EMU05 Experiment

The EMU05 experiment at CERN – Principal Investigator/Spokesperson, Y. Takahashi, The University of Alabama in Huntsville (UAH) – used 200 GeV / Nucleon sulfur beams for observation of high energy heavy-ion collisions with lead target. Almost all the emerging secondary charged particles were recorded with the Magnetic-Interferometric emulsion Chamber (MAGIC) in this experiment [67]. In the subsequent sections we adopt a left-handed Cartesian coordinate system to describe primary beam direction, orientation of emulsion plates reflecting the coordinate system defined in the automated stage microscope system used to carry out the measurements.

3.1.1 EMU05 Emulsion Chamber Configuration

Figure 3.1 shows the actual emulsion chamber configuration at the time of exposure to the sulfur beams. Table 3.1 shows the detailed chamber configuration.

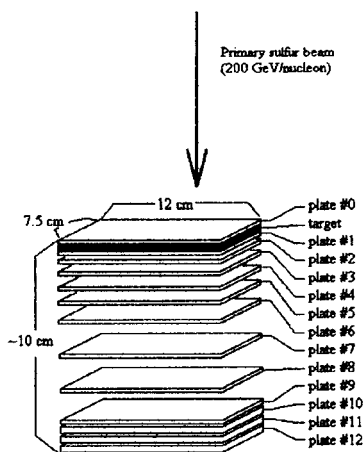


Figure 3.1 3-dimensional view of EMU05 emulsion chamber.

Table 3.1 EMU05 emulsion chamber configuration.

Material	Name	Type	Thickness (μm)
1	Glassine Paper		20
2	Emulsion Plate #0	I	400
3	Glassine Paper		20
4	Target Lead		200
5	Glassine Paper		20
6	Emulsion Plate #1	I	400
7	Glassine Paper		20
8	Lucite Plate		300
9	Glassine Paper		20
10	Emulsion Plate #2	I	400
11	Glassine Paper		20
12	Spacer		1,000
13	Glassine Paper		20
14	Emulsion Plate #3	I	400
15	Glassine Paper		20
16	Spacer		2,000
17	Glassine Paper		20
18	Emulsion Plate #4	I	400
19	Glassine Paper		20
20	Spacer		2,000
21	Glassine Paper		20
22	Emulsion Plate #5	I	400
23	Glassine Paper		20
24	Spacer		3,000
25	Glassine Paper		20
26	Emulsion Plate #6	I	400
27	Glassine Paper		20
28	Spacer		20,000
29	Glassine Paper		20

Table 3.1 (Continued)

Material	Name	Type	Thickness (μm)
30	Emulsion Plate #7	I	400
31	Glassine Paper		20
32	Spacer		20,000
33	Glassine Paper		20
34	Emulsion Plate #8	I	400
35	Glassine Paper		20
36	Spacer		20,000
37	Glassine Paper		20
38	Emulsion Plate #9	I	400
39	Glassine Paper		20
40	Emulsion Plate #10	II	770
41	Glassine Paper		20
42	Emulsion Plate #11	II	770
43	Glassine Paper		20
44	Emulsion Plate #12	II	770
45	Glassine Paper		20
<p>Type I Emulsion Plate: emulsion(50mm)+polystyrene(300mm)+emulsion(50mm)</p> <p>Type II Emulsion Plate: emulsion(350mm)+polystyrene(70mm)+emulsion(350mm)</p>			

One half of the MAGIC was exposed to one bunch of beam spill at the CERN SPS accelerator. The other half was exposed to another bunch of beam spill leaving two beam spots in emulsion plates, and the emulsion chamber was extracted from the beam line.

The MAGIC instrument uses a 200 μm thick lead plate as a target, thin emulsion plates (50 μm thick emulsion on both sides of 300 μm thick polystyrene plates) as a particle detector, and low density Styrofoam plates (1000 ~ 5000 μm thick) as spacers between emulsion plates. The target layer thickness was chosen to be 200 μm to reduce the production of electron pairs from γ -rays. The thickness of the emulsion layer was optimized at 50 μm in order to achieve visibility of individual tracks and to reduce secondary interactions in the emulsion layer. The base material polystyrene was chosen

for its high rigidity and low mass density. A few thick emulsion plates (700 μm thick) were placed at the most downstream of the chamber so that the particle identification could be done by grain density measurement. However, grain-counting measurements were not actually performed due to technical difficulties (limitation of available manpower for measurements). All the plates (12 cm \times 7.5 cm) were put in a black box (\sim 7 cm deep) and exposed vertically to the sulfur beam. A uniform 1.8 Tesla magnetic field was applied parallel to the emulsion plates so that the charge-sign and the momentum of each secondary particle can be obtained from the magnetic deflection of its track due to the Lorentz force. Figure 3.2 is the conceptual drawing of secondary particles traveling through MAGIC. Note that particle tracks are only recorded in emulsion layers. Therefore 3-dimensional event reconstruction is analogous to confocal imaging with coerce spacings.

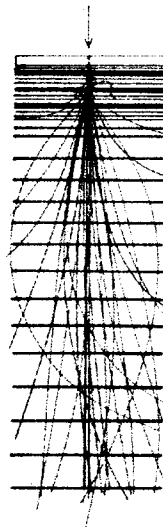


Figure 3.2 Conceptual drawing of tracks in MAGIC [2]. – The plane shown in this figure is vertical to the magnetic field.

In the coordinate measurement of secondary tracks recorded in the emulsion layer, an emulsion plate was placed on the microscope stage with high-precision step motors (in the x and y directions) and high-precision linear encoders. The following sections summarize the measurement procedures.

3.1.2 EMU05 Emulsion Plate Setting

The emulsion plate is placed on a 500 μm thick Lucite plate (20 cm \times 10 cm) with a guiding straight edge Lucite pieces attached on the surface perpendicularly (Figure 3.3).

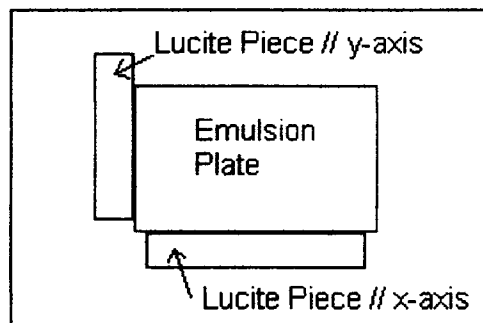


Figure 3.3 Emulsion plate setting on a Lucite plate.

The Lucite edges are used to align the plate so that the plate is always set parallel to the stage motion in x-direction. The accuracy of the alignment is

$$\tan \Delta\theta \leq 0.0001.$$

The emulsion layer is very sensitive to humidity and temperature change. In order to reduce errors and enhance visibility, emulsion plates must be set under the microscope carefully. Although all the measurements were performed in the air-conditioned laboratory room, the presence of an observer merely 30 cm away from the emulsion plate on the microscope stage changes the local environment surrounding the emulsion plate, which causes the emulsion plate to warp and consequently introduces misalignment of the Lucite base. Isolation of the emulsion plate from the rest of the room environment is implemented by a cover plate (12 cm \times 7.5 cm 0.1 mm thick Lucite plate) placed above the emulsion plate. The cover plate is taped down to 500 μ m thick Lucite base plate on all four sides. The entire plate is placed on the microscope stage at least 30 minutes before the measurement so that the emulsion plate is in thermal equilibrium and stable under the microscope. Usually 5 ~7 events in one beam spot are measured in one plate setting at the same time. The emulsion plate is removed from the Lucite base frame after the measurement and the next one is placed on the Lucite base frame and on the microscope stage in the same manner.

3.1.3 EMU05 General Scan

Figure 3.4 shows the distribution of two beam spots in one emulsion plate.

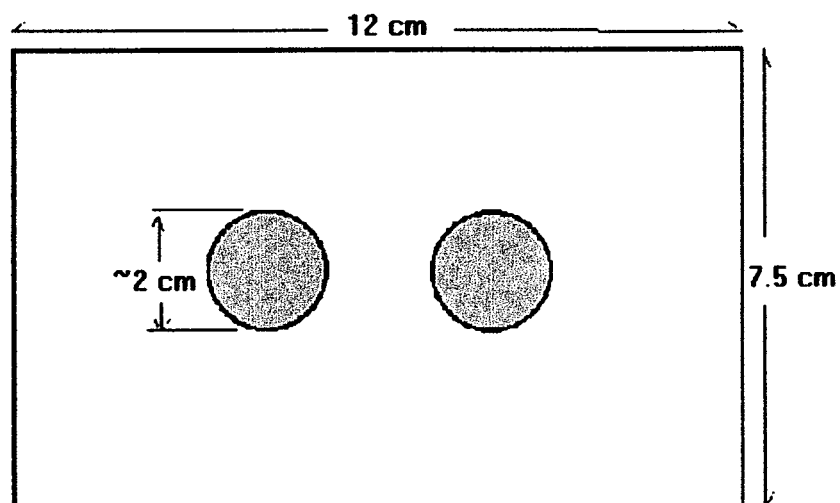


Figure 3.4 EMU05 beam spots recorded in the emulsion plate.

The typical distance between two adjacent sulfur beams is $\sim 30 \mu\text{m}$ in the most populated region in one beam spot. Although the emulsion layer's spatial resolution is submicron, one sulfur ion leaves a dark region with a diameter averaging $5 \mu\text{m}$ because of δ -rays. The average inter-beam distance of several tens of microns is large enough for unique identification of individual ion tracks (Figure 3.5).

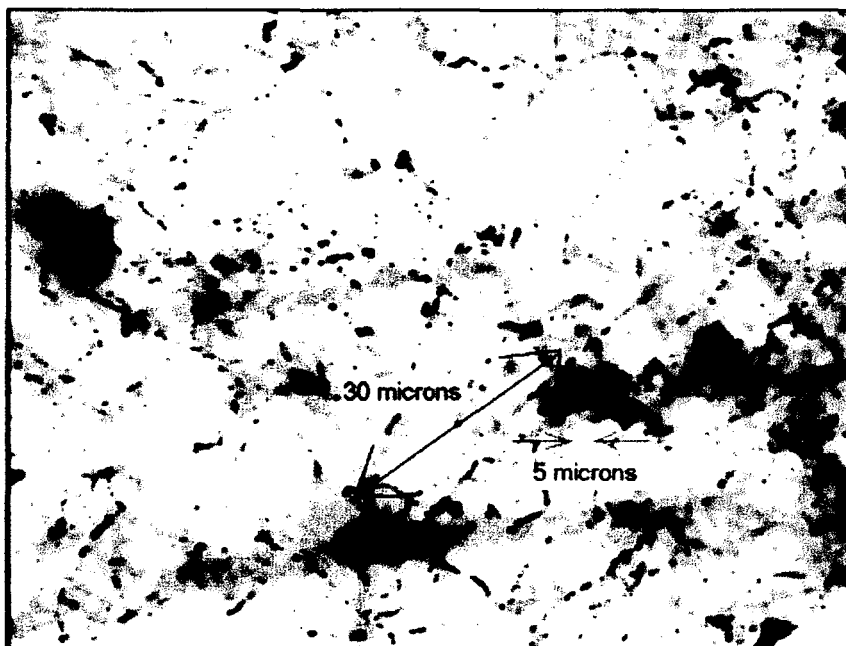


Figure 3.5 Typical non-interacting sulfur ion beam recorded in the emulsion plate #0 located upstream of the lead target.

The emulsion plate #0 (located upstream of the target lead plate) is first scanned for events by using low magnification objective lenses (10× or 20×). Rough estimates of multiplicities, vertex heights, and the locations of almost all the events were recorded for events which appear to have multiplicity larger than 100 to the observer. The emulsion plate consists of three layers – upstream emulsion layer (~50 μm), 300 μm polystyrene base plate, and downstream emulsion layer (~50 μm). The vertex height is estimated by the ratio of the radii of a few tracks with respect to the primary sulfur beam in the upstream emulsion layer and the radii of the corresponding track in the downstream emulsion layer using the triangulation formula:

$$\begin{aligned} &\text{upstream radius} : \text{downstream radius} \\ &= \text{vertex height} : (\text{vertex height} + 300\mu\text{m}), \end{aligned}$$

where vertex height is the vertical distance between the vertex of the interaction to the upstream polystyrene base surface.

The use of an upstream emulsion layer alone is avoided for vertex height estimation since the thickness of the emulsion layers at the time of exposure is not precisely known. Figure 3.6 shows a typical event in EMU05. The total multiplicity is estimated to be 250 ± 50 . The vertex height is estimated to be $130 \pm 10\mu\text{m}$ for this event.

This particular example shows a semi peripheral event, which indicates a few thick black tracks (nucleus fragments) as the characteristic symbols of a peripheral collision.

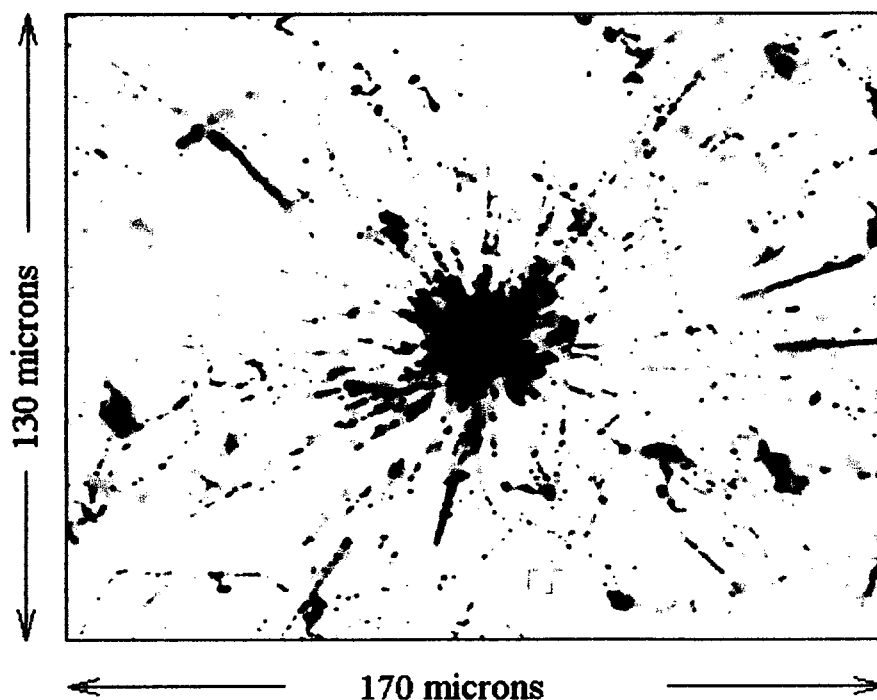


Figure 3.6 Image of a typical EMU05 event recorded in MAGIC. – The multiplicity of this event estimated prior to the track measurements is 250 ± 50 . A dark spot located near the left edge of the picture next to the number 130 is a non-interacting sulfur ion track.

3.1.4 EMU05 Event Selection

To select central collisions, the highest multiplicity events are selected by the estimated multiplicity. Ideally vertex heights (residual target thickness) should also be limited to within 50 microns for selecting events with fewer electron pair contamination arising from pair production in the residual target ($\gamma \rightarrow e^+e^-$). However, the number of events logged as the result of the general scan is about 20 to 30 in which the number of events with the multiplicity higher than 400 is limited to about 5 to 10. Therefore, only the estimated total event multiplicity was considered for event selection, and only events with estimated multiplicity > 400 are analyzed although the thick residual target creates a number of electron-positron pairs which will weaken the potential signals of isospin clustering among all the secondary tracks.

To make certain that the collision took place in the lead target and to estimate the vertex axis, the emulsion plate #0 (located upstream of the target lead plate) is observed. Only one out of 16 high multiplicity events was rejected because it was confirmed that the collision took place before primary sulfur ion entered into the lead target plate.

3.1.5 EMU05 Reference Beam Selection

Non-interacting sulfur ion tracks are used as the high-precision fiducial marks to determine the vertex axis within the accuracy of $\pm 1\mu\text{m}$ as the first step of the tracking procedure. In EMU05 about 50 non-interacting sulfur ion tracks are used. Figure 3.7 shows locations of reference beams of one of the analyzed events. Roughly half of the 50 tracks were chosen near the vertex axis for determination of the event center (crossing point of the vertex axis and the emulsion plate). The rest of the reference beams were taken from about 10,000 μm away from the event center in all four directions ($x \cong \pm 10,000 \mu\text{m}$, $y \cong \pm 10,000 \mu\text{m}$) for accurate determination of the plate alignment within $\tan \Delta\theta \leq 0.0001$. Reference beam locations for other events were selected by the same criteria. The unconventional coordinate system used in the figure reflects the left-handed coordinate system adopted in the microscope stage.

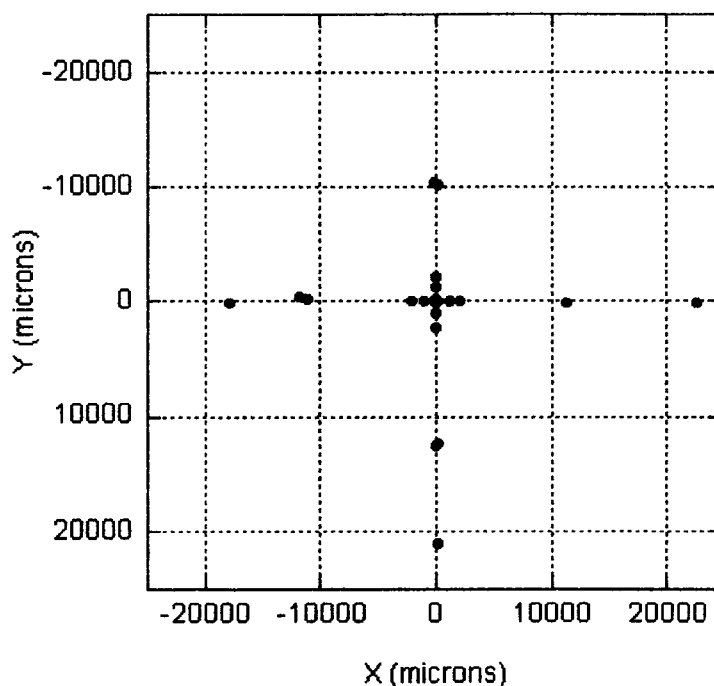


Figure 3.7 Typical location of reference beams selected for the estimate of translational and azimuth correction of emulsion plate setting.

3.1.6 EMU05 Tracking Procedure

Each track is traced downstream plate by plate. Two-dimensional coordinates of each track with respect to the parent beam axis (z axis) are measured with the microscope system: CUE-2 (Figure 3.8).

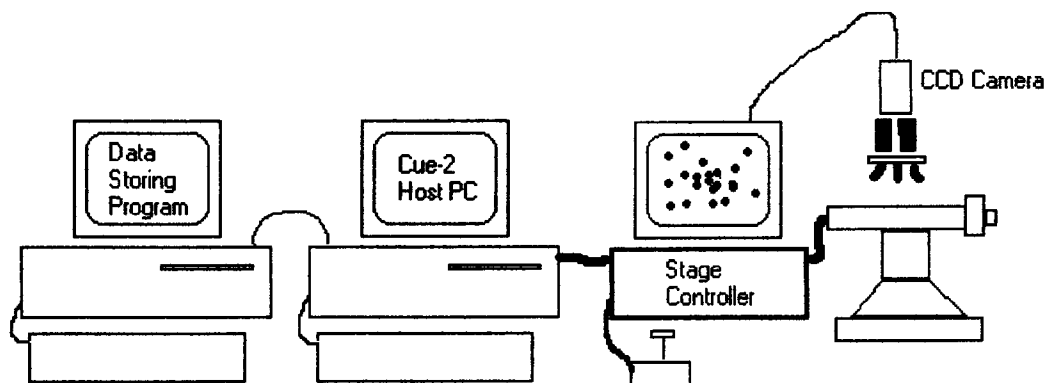


Figure 3.8 Schematic drawing of CUE-2 microscope system.

The emission angles ($\theta_{\text{LAB}}, \phi$) and the multiplicity became available after the first one or two plates were measured ($z < 1000\mu\text{m}$ downstream from the vertex.) In order to obtain charge-signs and momenta, individual tracing must be done throughout the emulsion spectrometer down to $z \approx 7$ cm. First, the emulsion plate #0 is measured for the primary beam location with respect to the selected reference beams. Next, the emulsion plate #1 is placed under the CUE-2 microscope system. The image taken by the CCD camera in the plane $1\mu\text{m}$ above the upstream surface of the base polystyrene plate is shown on the screen. The picture shown in Figure 3.6 was thus taken. The emulsion plates are designed as described in the Section 3.1.1 to minimize the secondary particle interactions within the medium while maintaining the precise record of the trajectory. The design of an emulsion plate - double emulsion layers coated on both sides of a solid polystyrene base plate - was thus chosen to provide rigid planes for precise xy -coordinate measurements. The emulsion layer's thickness has a relatively large uncertainty of $50 \pm 10 \mu\text{m}$ at the time of exposure, but the location of the track at the interface with the base plate gives a sub-micron precision for x - and y -coordinates. Each secondary track's location is, therefore, measured by the closest grain to the polystyrene base plate.

One pixel overlay mark ($\sim 1/5$ of the actual grain size in the image taken via $50\times$ objective lens) is left at the center of each track. The original image is then erased leaving the overlay only on the screen. The CUE-2 image analyzer takes x and y coordinates of all the overlay marks within one screen. The xy -coordinates are recorded in the data storing program called "JCYEN.BAS" written in BASIC computer language

(Appendix A). The microscope stage is then moved to show the next frame adjacent to the central frame. The new image center has an offset of $\Delta x = 85 \mu\text{m}$ and $\Delta y = 65 \mu\text{m}$, equivalent to the stepping size of one frame, which are added or subtracted from the new image's local coordinates in order to record the secondary track's xy coordinates relative to the event center. The new image is then measured by the same method as the central image frame. A total of 9 image frames (1 center frame + 8 surrounding frames) is measured by the CUE-2 image analyzer. These 9 frames cover almost 90% of the secondary particles in emulsion plate #1.

Tracks with larger emission angles which are not seen in the 9 image frames are measured by bringing the center of the grain, one closest to the polystyrene base plate, to the center of the central image frame and reading xy coordinates from the linear encoders attached to the microscope stage. Tracks near the event center are usually highly populated, and it is not possible to distinguish them all in the upstream emulsion layer of plate #1. However in the downstream emulsion layer, they are well separated and an individual track becomes clearly separable. Figure 3.9 shows the image of a downstream emulsion layer of the same event as shown in Figure 3.6. The relatively large black track appearing in the lower left corner is the same non-interacting sulfur ion beam as shown in Figure 3.6. Several center most tracks, which are not distinguishable in the upstream emulsion layer, become visible in this downstream emulsion layer. Coordinates of these tracks are added to the JCYEN data base via similar CUE-2 image analysis method.

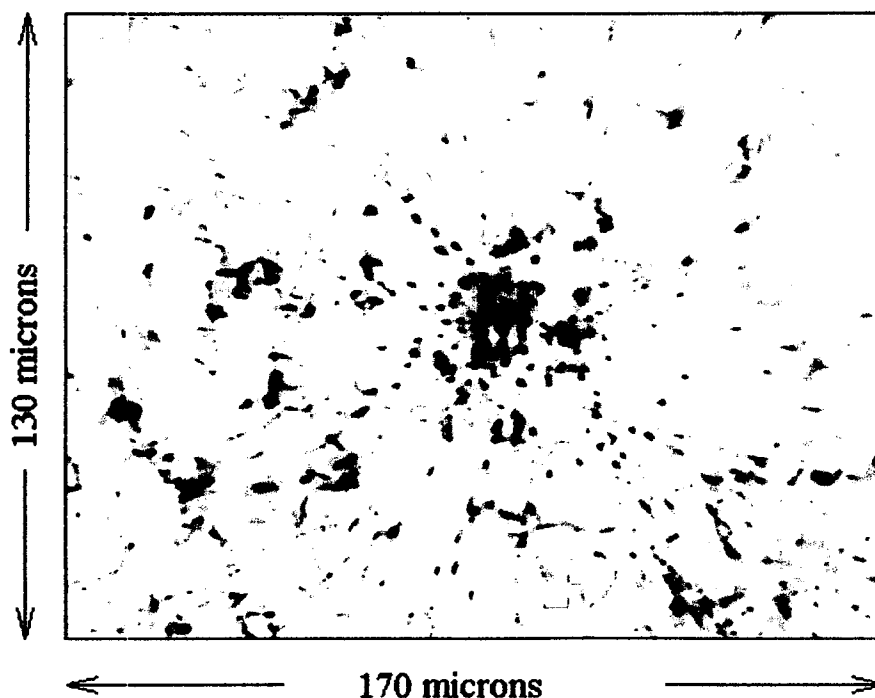


Figure 3.9 Image of the same event as shown in Figure 3.6. – The non-interacting sulfur ion track is still visible on the left edge of the picture.

In emulsion plate #1 placed less than 200 μm downstream from the vertex point, one can safely ignore magnetic deflections. After measuring tracks in emulsion plate #1, we can determine the vertex axis and the vertex height by the least square fit, using the measured tracks of the secondary particles. The translational error in determination of the vertex location is less than 1 μm at this stage. When all the secondary particles were measured for xy-coordinates in emulsion plate #1, emulsion plate #2 is placed under the microscope, replacing plate #1. The data storing program, JCYEN.BAS, is capable of predicting the track location in the subsequent emulsion plate, #2, using the information such as the vertex height, the event center, and the emission angles, obtained from emulsion plate #1, such as vertex height, event center, and emission angles. Each track found in emulsion layer #1 is sought in emulsion plate #2 and the xy-coordinates of the corresponding track are recorded manually by reading off the xy-coordinates of the linear encoder each time. Whenever the position of the last grain was recorded in the upstream emulsion layer, the microscope stage was moved back to the position of the central cursor of the central image frame, where the coordinate-referencing system-values were confirmed.

The multiplicity for the central collision of 200 GeV/nucleon sulfur and lead is more than 500. The measurement step described above is repeated more than 1000 times ($= 500 \times 2$ times for upstream and downstream emulsion layers) for one emulsion plate. The recorded xy-coordinate information obtained from emulsion plate #2 is iterated into the least-square fit vertex height and event center determination. The tracking is carried out in this manner up to emulsion #5 which is located about 10,000 μm downstream from a vertex.

Downstream of emulsion plate #5, most of the secondary tracks start to deflect significantly from its predicted location by linear-fitting, and the track location prediction by the linear-fitting becomes no longer valid. Starting at the downstream layer of emulsion plate #5, a circular curve fitting is used to predict the track location in the next plane. The timing of switching the prediction method is determined by the trained observer's intuition while maintaining the linear-fitting prediction method to non-deflecting y-coordinates. Generally speaking, if the momentum of a particle is low, its linear-fitting prediction starts to accumulate deviation from its measured x-coordinate because of the magnetic deflection. Considering these characteristics, the prediction method is switched to a curvature-fitting method as early as emulsion plate #3. On the other hand, if the momentum of a particle is high, the linear-fitting prediction stays valid up to emulsion #6, which is 3,000 μm downstream of emulsion plate #5, because the curvature is too large to fit a circle using only a few measured points. Hence emulsion plate #5 (before 3,000 μm "jump") is regarded as the most critical emulsion plate in MAGIC. If a track is not found, or both linear-fitting and circular-fitting errors for a new measured point in emulsion plate #6 increase, the lost track is searched again in emulsion plate #5. At most only a few tracks are lost between emulsion plates #5 and #6 in measurements by a trained observer. The circular curvature becomes well established after the measurement of tracks in emulsion plate #6 regardless of the particle's momentum. Measurements in emulsion plate #7 work well with the circular fit prediction. At this point both charge-sign and momentum of each particle is already well determined. The tracks in emulsion plates #8 and #9 are measured in order to confirm the curvature fit and to further improve the accuracy of the momentum determination.

3.1.7 EMU05 Tracking efficiency and precision

Almost all the tracks can be traced through the entire emulsion spectrometer, except those tracks (i) going out of the chamber, (ii) scattered with large angles, and (iii) decayed particles. Present measurements have shown that the efficiency of tracking the particles throughout the detector for the determination of charge-signs is better than 90%, averaging 96 % for all particles.

We note here the general precision of the coordinate measurements. First, the spatial resolution in the emulsion film is sub-micron determined by the grain size (diameter ~ 0.24 microns). The combination of the errors in automated stage motion and of the image analyzer itself is applied to evaluate the accuracy of measurements. The latter has the resolution of sub-micron ($\sim 0.5 \mu\text{m}$), and although the former has mechanical backlash errors, a feed back from the encoder, working independently from the stage driving motor, minimizes the errors to $\pm 0.5 \mu\text{m}$ in a few successive stage motions of $\pm 10000 \mu\text{m}$ in both x and y directions. Although the reference beams have the size as large as a few microns, a sufficiently large amount of references are taken (~ 50) and their statistical overall spatial resolution is estimated to be $\sim \pm 0.5 \mu\text{m}$ (Figure 3.10). Considering the spatial resolutions mentioned above and the precision of the machine processed plastic base plate, the angular resolution in one emulsion plate is better than ± 0.10 deg in EMU05.

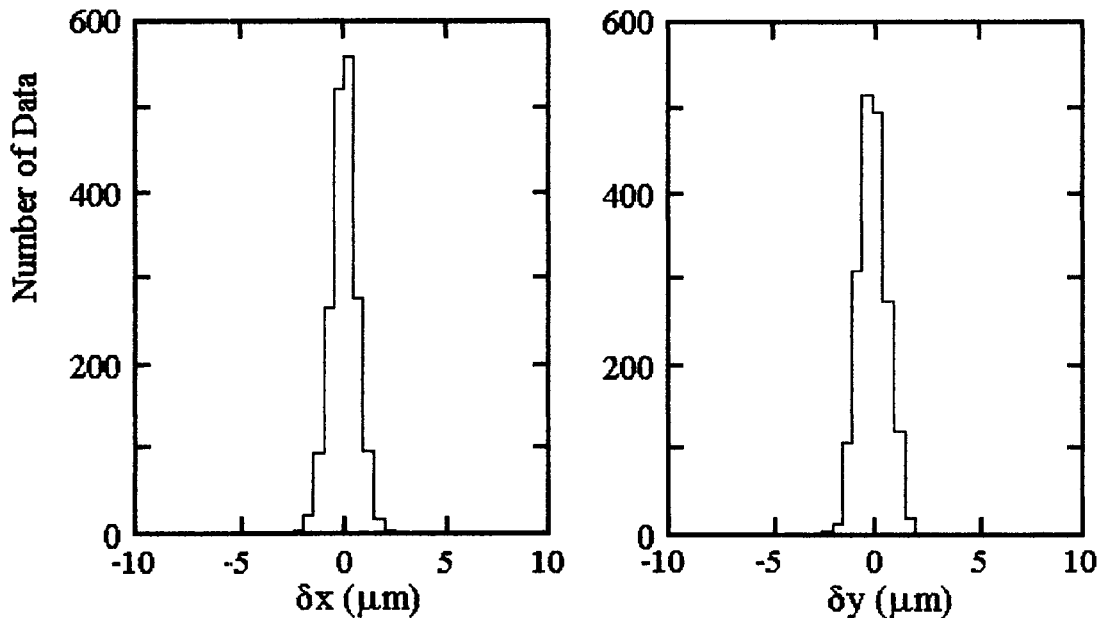


Figure 3.10 Translational error of reference beams.

3.1.8 EMU05 Momentum Resolution

The precision of the momentum determination depends on the chamber design (multiple scattering) and the momentum itself (limited by the spatial resolution of the magnetic deflection curvatures). It is found from the data set of several thousand measured tracks that the momentum precision is fit well to the formula:

$$\Delta p/p = 5 + [p/(20\text{GeV}/c)]\%$$

for the momentum range 0.2 GeV/c to 200 GeV/c.

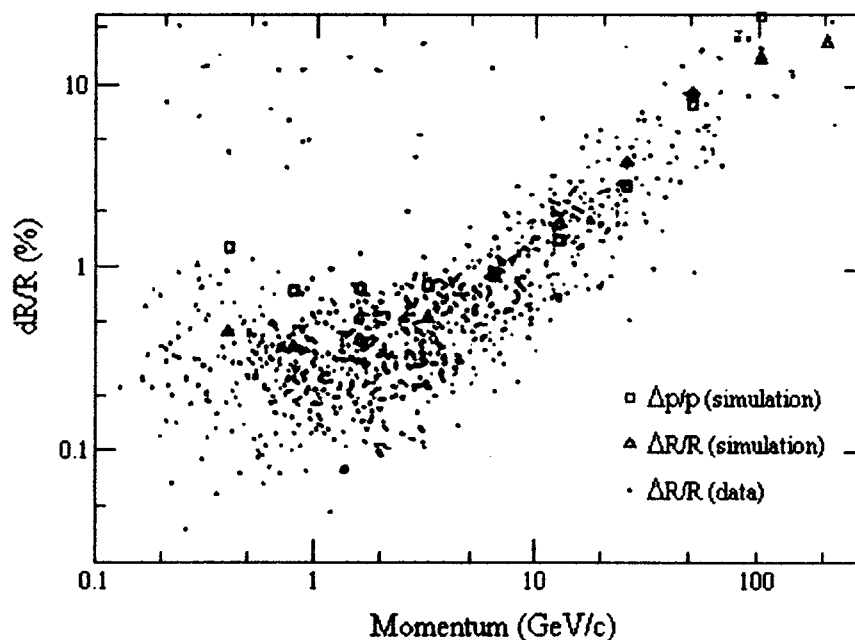


Figure 3.11 EMU05 momentum precision [68].

§3.2 CERN EMU09 Experiment

The CERN EMU09 experiment (Spokesperson: G. Romano, Univ. of Salerno, Italy) was operated at the same time as EMU05 [69]. The EMU09 used the same sulfur beam and similar emulsion chambers as MAGIC. Despite the similarity of the emulsion chamber configuration, the primary goal of EMU09 was charmed particle detection, so the chamber and its operation were not optimized for acquisition of all charged particle spectra as in EMU05. Similarities and differences noting advantage and disadvantage of EMU09 emulsion chamber are described in this section.

3.2.1 EMU09 Emulsion Chamber Configuration

Figure 3.12 shows the emulsion chamber design of EMU09. Emulsion plates #1, #2, #4, and #6 are inserted in addition to the nominal design of EMU09.

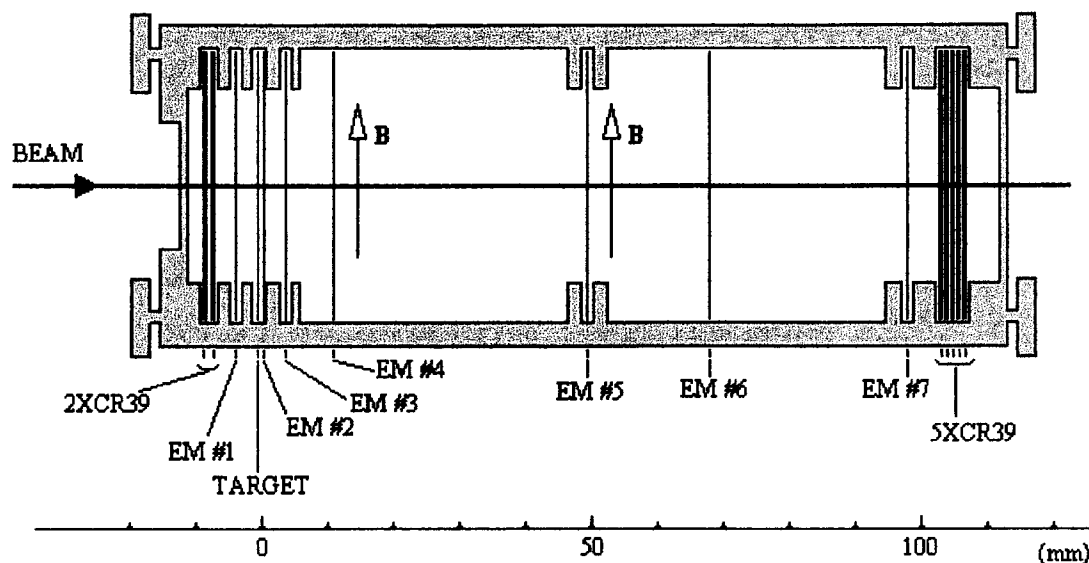


Figure 3.12 Vertical view of EMU09 emulsion chamber [69].

The chamber was constructed in a hollow black plastic box, and the emulsion plates (10 ~ 30 μm thick emulsion layers on both sides of 200 μm thick polystyrene plates) were bolted in slots (24.5 cm \times 4.5 cm) with no mechanical supports in the middle. Consequently the emulsion plates have a slight warp which requires additional adjustment. A uniform 2.47 Tesla magnetic field was applied parallel to the emulsion plates for momentum and charge-sign determination. Table 3.2 lists the configuration of the EMU09 emulsion chamber. The EMU09 emulsion chamber was exposed to the sulfur beam differently from EMU05. The emulsion chamber was moving across the beam line during the exposure to reduce the event rate per unit area of the emulsion plates. This made a heavily populated area at the edge of the emulsion plate about 1cm inside of the edge and a less populated narrow band in between as shown in Figure 3.13. In the following EMU09 tracking procedure sections, the difference from the EMU05 is emphasized.

Table 3.2 EMU09 emulsion chamber configuration.

Material	Name	Type	Location
1	emulsion plate #1	I	upstream of target
2	Target Lead	50 μ m	Target
3	emulsion plate #2	I	at ~100 μ m from target
4	emulsion plate #3	I	at ~3,400 μ m from target
5	emulsion plate #4	I	at ~9,300 μ m from target
6	emulsion plate #5	I	at ~49,700 μ m from target
7	emulsion plate #6	I	at ~70,000 μ m from target
8	emulsion plate #7	I	at ~100,100 μ m from target

Type I Emulsion Plate:
emulsion (30 μ m) + polystyrene (200 μ m) + emulsion (30 μ m)

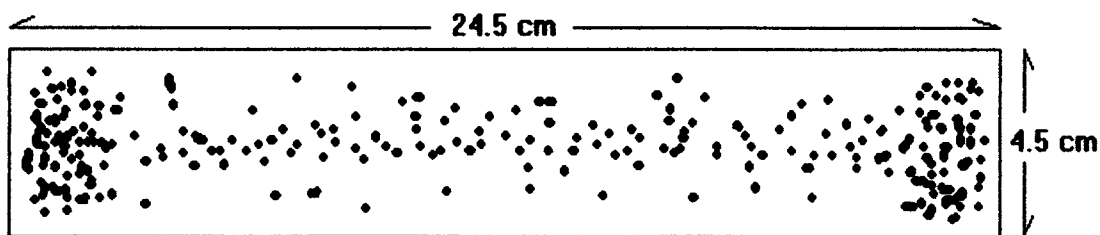


Figure 3.13 EMU09 primary sulfur ion beam population.

3.2.2 EMU09 Plate Setting

EMU09 emulsion plates are mounted directly on to a glass plate (thickness ~5 mm dimension ~30 cm \times ~30 cm). Isolation from the room environment is achieved similarly by a 100 μ m thick clear Lucite plate and Scotch tape as the EMU05 emulsion plates used. The precision of the alignment is similarly maintained as EMU05:

$$\tan \Delta\theta_{\text{LAB}} \leq 0.0001.$$

Four emulsion plates are mounted on the glass plate at a time – plates #1, #2, #3, and #4 for upstream tracking and plates #4, #5, #6, and #7 for downstream tracking (Figure 3.12 and Table 3.2). The emulsion #4 is mounted for both upstream and downstream tracking for the convenience of going back and forth between layers.

3.2.3 EMU09 General Scan

The number of events is proportional to the number of primary sulfur ions. The majority of events exist in the highly populated far right and far left regions. In order to

reduce the number of particles going out of the emulsion spectrometer in the downstream layer in the vicinity of events, events are scanned only at the central narrow band of the primary sulfur beams. A rough multiplicity count is performed to select for central-collision events, which should have about the same multiplicity of 400 or more as in EMU05. The typical distance between the two adjacent sulfur beams is $\sim 200 \mu\text{m}$ in the center narrow band of the primary sulfur beam population.

Although the emulsion layer's spatial resolution is less than $1 \mu\text{m}$, one sulfur ion leaves a dark region with a diameter averaging $3 \mu\text{m}$ because of δ -rays. The average inter-beam distance is large enough for the identification of an individual ion track. Emulsion plate #2 (located downstream of the target lead plate) is scanned for events by using low magnification objective lenses ($10\times$ or $20\times$). Rough estimate of multiplicities, vertex heights, and the locations of almost all the events are recorded for events which appear to have multiplicity larger than 400 to the observer.

All the emulsion plates used in EMU09 consist of three layers – upstream emulsion layer ($\sim 30 \mu\text{m}$), $200 \mu\text{m}$ polystyrene base plate, and downstream emulsion layer ($\sim 30 \mu\text{m}$). The vertex height is estimated by the ratio of the radii of a few tracks with respect to the primary sulfur beam in the upstream emulsion layer and the radii of the corresponding track in the downstream emulsion layer using the following triangulation formula, similar to that of EMU05:

$$\begin{aligned} &\text{upstream radius} : \text{downstream radius} \\ &= \text{vertex height} : (\text{vertex height} + 200 \mu\text{m}), \end{aligned}$$

where vertex height is the vertical distance between the vertex of the interaction to the upstream polystyrene base surface.

3.2.4 EMU09 Event Selection

To select central collision events, the highest multiplicity events are selected by the estimated multiplicity. The total number of events selected in the EMU09 emulsion chamber is 11. Since the number of high multiplicity events is a constant fraction of the total number of the primary beams, there are more high multiplicity events located at the edge-most large beam population areas. However thick dark tracks of non-interacting primary beams in the vicinity of an event make it nearly impossible to track single charge tracks downstream, and the majority of the particles had escaped from the emulsion chamber before we could establish the accurate charge and momentum determination.

Therefore events are selected only from the less densely populated center of the emulsion plate.

3.2.5 Reference Beam Selection

Non-interacting sulfur ion tracks are used to determine the vertex axis within the accuracy of $\pm 1 \mu\text{m}$ as the first step of the tracking procedure. In EMU09 about 100 non-interacting sulfur ion tracks are used as shown in Figure 3.14.

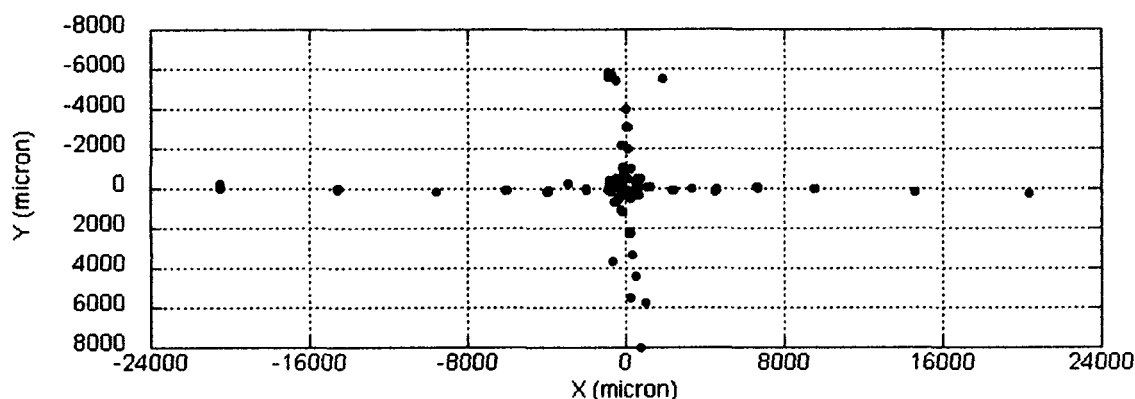


Figure 3.14 Typical location of reference beams selected for estimate of translational and azimuth alignment of emulsion plate setting (EMU09).

Procedures for reproducing the geometry of the exposure are similar to those in the EMU05 procedures already described in Section 3.1. About 50 beam tracks were used near the vertex axis for determination of the event center (crossing point of the vertex axis and the emulsion plate). About 50 more reference beams are selected at the locations far away from the event center in all four directions ($x \cong \pm 20,000 \mu\text{m}$, $y \cong \pm 10,000 \mu\text{m}$). This provided a sufficient accuracy for the determination of the plate alignment within the error: $\tan \Delta\theta \leq 0.0001$.

3.2.6 Tracking Procedure

The tracking procedure in the EMU09 emulsion chamber is almost identical to that of EMU05. The major difference is that the transition point from linear-fitting prediction to circular-fitting prediction is between emulsion plates #3 and #4 where a large gap of over 8mm ($8,000 \mu\text{m}$) made the tracking procedure rather inefficient. In fact, it was extremely difficult to find corresponding tracks in emulsion plate #4.

Using the experience earned in EMU05 measurement and learning systematic y coordinate prediction error, a trained observer was able to trace secondary tracks over the 8mm jump with little technical difficulty and high level of confidence. Once tracks are found in emulsion layer #4, the circular-fitting prediction becomes accurate enough to go to the next large gap (4 cm jump) between emulsion plates #4 and #5. When a track is not found at the predicted area in plate #5, plate #4 is searched again for improvement of the fitting of the track curvature. However, the observer needs to be very careful not to record the same track for different particles. Confirmation was made by reviewing all xy coordinates recorded in the JCYEN.BAS program for predicting the position in the subsequent layer after completing all measurements in one emulsion plate. The tracking efficiency remains still almost 98% except for the tracks leaving the emulsion chamber. After the measurements in emulsion plate #5, the curvature of a track is well determined so that the tracing in plates #6 and #7 is performed for confirmation of the fitted curvature and for improvement of the momentum determination.

3.2.7 EMU09 Tracking Efficiency and Accuracy

Almost all the tracks were traced through the entire EMU09 emulsion spectrometer, except tracks going out of the chamber ($\theta_{\text{LAB}} > 15^\circ$: ~ 25% of all secondary particles) and large-angle scattered tracks. By the same argument made for EMU05 in Section 3.1.7, the angular resolution in one emulsion plate was better than ± 0.14 deg for EMU09.

3.2.8 EMU09 Momentum Resolution

The expected momentum error in EMU09 data is

$$\Delta p / p = 3 + [p / (20 \text{ GeV} / c)] \%$$

Figure 3.15 shows momentum determination precision of EMU09.

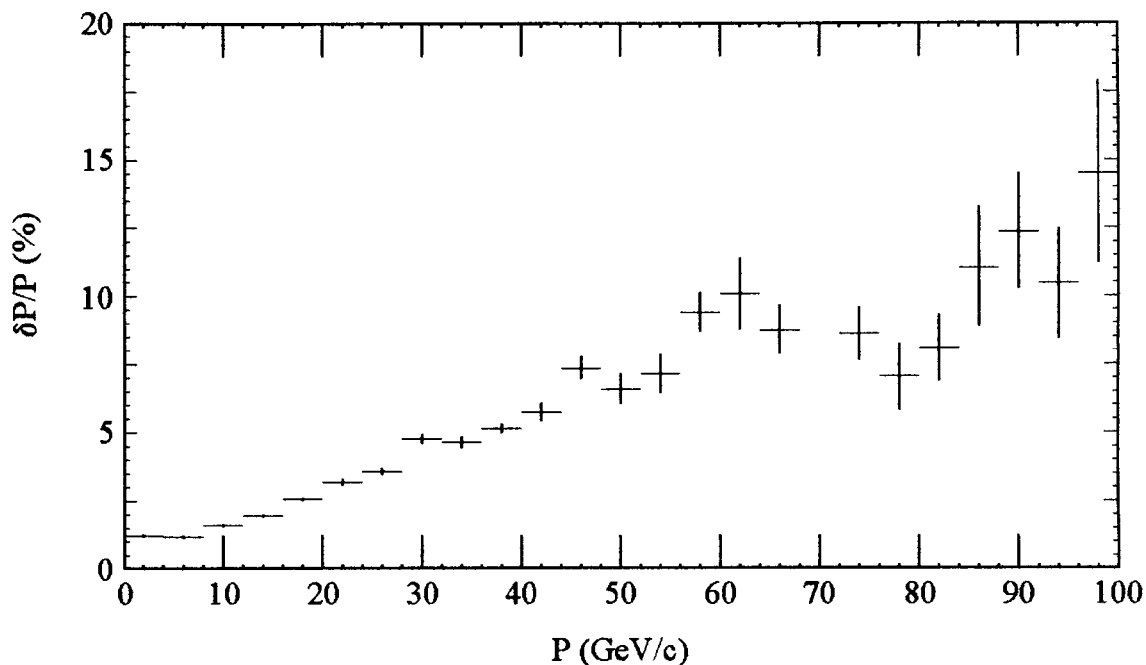


Figure 3.15 EMU09 momentum precision [70]

§3.3 CERN EMU16 Experiment

The CERN EMU16 experiment (Spokesperson Y. Takahashi, UAH) [70] used 158 GeV / Nucleon lead beams. As in the EMU05 experiments, almost all the emerging secondary charged particles were recorded with the very similar Magnetic-Interferometric emulsion chamber to that of the EMU05 experiment. One half of MAGIC was exposed to one bunch of the beam spill at the CERN SPbS accelerator. The other half was exposed to another bunch of beam spill leaving two beam spots in emulsion plates, and the emulsion chamber was extracted from the beam line.

3.3.1 EMU16 Emulsion Chamber Configuration

The EMU16 MAGIC used a 200 μm thick lead plate as a target, thin emulsion plates (50 μm thick emulsion on both sides of 300 μm thick polystyrene plates) as particle detectors, and low density Styrofoam plates (1000 ~ 5000 μm thick) as spacers between emulsion plates. Part of the spacer (Styrofoam) was cut out where lead ion beams were expected to go through. This treatment further reduced the occurrence of unwanted secondary interactions in the spacer Styrofoam. The target layer thickness was chosen to be 200 μm to reduce the production of electron pairs from γ -rays. The thickness of the emulsion layer was 50 μm in order to achieve visibility of individual tracks and to minimize the occurrence of the secondary interactions in the emulsion layer. Polystyrene

was used for the emulsion substrate. All the plates (12 cm \times 7.5 cm) were put in a black box (\sim 7 cm deep) that was used in EMU05 and exposed vertically to the sulfur beam in exactly the same way as EMU05. Table 3.3 shows the detailed emulsion chamber configuration.

A uniform 1.8 Tesla magnetic field was applied parallel to the emulsion plates so that the charge-sign and the momentum of each secondary particle could be obtained from the magnetic deflection of its track due to the Lorentz force. In the coordinate measurement of secondary tracks recorded in the emulsion layer, an emulsion plate was placed on the microscope stage with high-precision step motors (in x and y direction) and high-precision linear encoders. The following sections summarize the detailed measurement procedures.

Table 3.3 EMU16 emulsion chamber configuration table.

Material	Name	Type	Thickness (μm)
1	Glassine Paper		20
2	Emulsion Plate #0	II	400
3	Glassine Paper		20
4	Target Lead		200
5	Glassine Paper		20
6	Emulsion Plate #1	I	300
7	Glassine Paper		20
8	Lucite Plate		300
9	Glassine Paper		20
10	Emulsion Plate #2	II	400
11	Glassine Paper		20
12	Spacer		1,250
13	Glassine Paper		20
14	Emulsion Plate #3	II	400
15	Glassine Paper		20
16	Spacer		2,500
17	Glassine Paper		20
18	Emulsion Plate #4	II	400
19	Glassine Paper		20
20	Spacer		2,500
21	Glassine Paper		20
22	Emulsion Plate #5	II	400
23	Glassine Paper		20
24	Spacer		5,000
25	Glassine Paper		20
26	Emulsion Plate #6	II	400
27	Glassine Paper		20
28	Spacer		10,000
29	Glassine Paper		20
30	Emulsion Plate #7	II	400

Table 3.3 (Continued)

Material	Name	Type	Thickness (μm)
31	Glassine Paper		20
32	Spacer		20,000
33	Glassine Paper		20
34	Emulsion Plate #8	II	400
35	Glassine Paper		20
36	Spacer		30,000
37	Glassine Paper		20
38	Emulsion Plate #9	II	400
39	Glassine Paper		20
40	Spacer		30,000
41	Glassine Paper		20
42	Emulsion Plate #10	II	400
43	Glassine Paper		20
44	Spacer		30,000
45	Glassine Paper		20
46	Emulsion Plate #11	II	400
47	Glassine Paper		20
48	Emulsion Plate #12	III	700
49	Glassine Paper		20
50	Emulsion Plate #13	III	700
51	Glassine Paper		20
52	Emulsion Plate #14	III	700
53	Glassine Paper		20
<p>Type I Emulsion Plate: emulsion(50mm)+polystyrene(300mm)+emulsion(50mm)</p> <p>Type I Emulsion Plate: emulsion(50mm)+polystyrene(300mm)+emulsion(50mm)</p> <p>Type I Emulsion Plate: emulsion(50mm)+polystyrene(300mm)+emulsion(50mm)</p>			

3.3.2 EMU16 Plate Setting

Because EMU16 uses emulsion plates of the same dimension as those used in EMU05, the plate setting is exactly the same as EMU05.

3.3.3 EMU16 General Scan

The distribution of two beam spots is almost the same as EMU05. The beam intensity was about 9 times higher than the sulfur beam used in EMU05. The typical distance between two adjacent lead beams is $\sim 10 \mu\text{m}$ in the most populated region in one beam spot. General scans for central events were performed on emulsion #1 placed just below the target lead plate. Several high multiplicity events ($N_{ch} > 1000$) were observed in one beam spot.

The #1 emulsion plate consists of three layers – upstream emulsion layer ($\sim 50 \mu\text{m}$), $300 \mu\text{m}$ polystyrene base plate, and downstream emulsion layer ($\sim 50 \mu\text{m}$). The vertex height is estimated by the ratio of the radii of a few tracks with respect to the primary sulfur beam in the upstream emulsion layer and the radii of the corresponding track in the downstream emulsion layer using the formula (same as EMU05):

$$\begin{aligned} & \text{upstream radius} : \text{downstream radius} \\ & = \text{vertex height} : (\text{vertex height} + 300\mu\text{m}), \end{aligned}$$

where vertex height is the vertical distance between the vertex of the interaction to the upstream polystyrene base surface.

3.3.4 EMU16 Event Selection

Although the linear size of a lead ion is twice as large as a sulfur ion, grain density also depends on the emulsion film development condition. The diameter of a typical lead ion track in an EMU16 emulsion plate is $\sim 2 \mu\text{m}$. However, event selection is not performed only on total event multiplicities for EMU16. Because of the higher primary lead beam intensity, neighboring non-interacting lead ions overlap with some of the single charged secondary particles, which creates a similar problem as in the highly populated edge-most spots in EMU09. Therefore, only one high multiplicity event is selected from the lower right quadrant of one right beam spot for analysis, where the primary sulfur ion beam distribution density is smaller.

3.3.5 Reference Beam Selection

Due to the location of the event in the beam spot, the reference beams were selected asymmetrically as shown in Figure 3.16. 77 non-interacting lead ion beams

were selected as reference. The unconventional coordinate system used in the figure reflects the left-handed coordinate system adopted in the microscope stage.

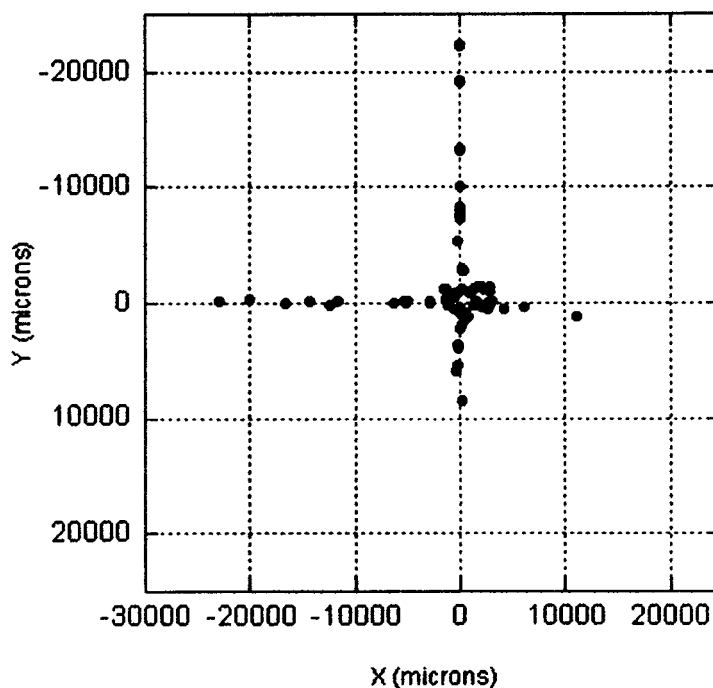


Figure 3.16 EMU16 reference beam selection. – Abscissa is for the x coordinate, and ordinate is for the y coordinate.

3.3.6 EMU16 Tracking Procedure

The tracking procedure is almost identical as that of EMU05. The only difference is that the event is divided into 4 quadrants to reduce the number of entry of secondary particles in one set of measurements. This is due to the limitation of the multiplicity handling capability of the data storing program, JCYEN.BAS, and also for quick event profile determination assuming the event is symmetrical around a primary parent beam axis. All 4 quadrants are measured in the same manner and added to form one data set. In all 4 quadrants, the same 77 reference beams are shared.

3.3.7 EMU16 Tracking Efficiency and Precision

It is assumed that the tracking precision is the same as that of EMU05. However, the tracking efficiency decreased almost by a factor of two for all secondary particles in the lower right quadrant ($x \geq 0, y \geq 0$) due to the inconvenient location of the event center with respect to the emulsion plates. However, the charge-sign of each track is determined very well before the tracks left the emulsion chamber.

3.3.8 EMU16 Momentum Resolution

It is assumed that the momentum resolution is the same as that of EMU05.

§3.4 Comparison of Emulsion Experiments – EMU05, EMU09, and EMU16

The following summarizes a few features of EMU09 compared to EMU05 or EMU16.

advantages

- i) The magnetic field applied to the emulsion chamber is stronger (2.47 Tesla). The maximum observable particle momentum is higher and the curvature fitting accuracy is better than those in the EMU05 experiments in general.

- ii) The depth of the chamber is larger (~10 cm). The maximum observable particle momentum is higher and the curvature fitting accuracy is better than the EMU05 values in general.

- iii) The amount of material in a chamber is less (6 emulsion plates after the target and no spacer material). Less multiple-scattering introduces less errors in momentum determination of the observed secondary particles.

disadvantages

- iv) The emulsion plates are narrower (4.5 cm × 2.4 cm) than those of EMU05. Particles with wide emission angles cannot be observed in the downstream emulsion plates.

- v) The emulsion layer is thinner by a factor of 2, and the grain density is smaller. It is very difficult to identify individual tracks in one emulsion plate. Constant reconfirmation of tracks in neighboring emulsion plates is required.
- vi) The number of available events is less (~15 events total). The event rate and the primary sulfur beam intensity is comparable with EMU05. However, due to the way that the emulsion chamber was exposed during the beam run, the majority of events are located at the edge of the emulsion plate. In this measurement those events located in the edge region were avoided to lessen lost tracks in downstream emulsion layers and to optimize the visibility of tracks.
- vii) Most of the emulsion plates are slightly warping. Particle tracking in EMU09 emulsion plates requires a trained observer's intuition on the pattern of the warp during the particle tracking and systematic correction on the xy coordinate of the reference beams and secondary particles after the measurement.

The observer had a good microscope system with a high-precision stage, controlled by computerized stage-drivers and linear encoders. The UAH emulsion microscope laboratory provided this equipment. The emulsion experiments with high-energy heavy-ion beams offer a precise determination of coordinates of secondary particles, and consequently, permit measurements of momentum of all the particles in individual interactions. This capability uniquely provided the all-particle data with charge-sign (isospin of pions) and momentum known for almost all the produced individual particles. Thus, the UAH emulsion experiments became the sole source of the all-particle data set for the research field of multi-particle dynamics at high energy densities.

In the following sections, inclusive and semi-inclusive cross sections are presented. The particular analysis of the charge-sign clustering is described in Chapter 4 with the details of the statistical analysis methods. The multi-particle data obtained in EMU05, EMU09, and EMU16 experiments as described in Section 3.1 through 3.4, are used in search of Disoriented Chiral Condensate in terms of charge-sign cluster analysis.

§3.5 Inclusive Spectra

The number of events, observed with precise coordinate measurements, is 16 EMU05 200 GeV/nucleon S + Pb central events, 11 EMU09 200 GeV/nucleon S + Pb

events, and 1 EMU16 158 GeV/nucleon Pb + Pb event. Unfortunately 3 data sets of EMU05 were lost by accident. We include an additional 17 events of EMU05 200 GeV/nucleon S + Pb in the present data analysis. (Those events were obtained in the first run of sulfur ion beam (200 GeV/nucleon) at CERN in 1986 and measured by A. Iyono [68] by the same precise coordinate measurement using a microscope system similar to the one that was used at UAH.) The additional data are also used in the canonical Fourier multiparticle charge-sign clustering analysis which will be described in detail in Chapter 4. In this section we present the inclusive data that we obtained in EMU05, EMU09, and EMU16 and how the data is utilized for the canonical Fourier analysis with its capability.

3.5.1 Pseudorapidity – Azimuth Angle Distribution (particle by particle)

Due to the volume of the plots, pseudorapidity – azimuth distributions (η – ϕ distributions) plots for all observed events of EMU05, EMU09, and EMU16 are listed in APPENDIX A (Figures A.1 through A.42). All particles measured in one event are plotted in one drawing – open circles for a positively charged particles and open squares for a negatively charged particles. Small dots represent particles of which the charge signs were not determined because of large errors in curvature fitting, insufficient data points, and/or because the particle tracks did not converge to the vertex well enough (“impact parameter” cut). The “impact parameter” we use in our analyses is the distance between the vertex point on the primary beam axis and the intersection of beam axis and fitted curvature of the track of a particle. We chose 6 μm to be the maximum allowable “impact parameter.” The reason to impose the cut by this criterion of the “impact parameter” is the fact that there is some contamination of electrons and positrons in the measured charged tracks. Those particles whose tracks cross the vertex axis at a distance larger than 6 μm are considered to be electrons or positrons converted in the residual target lead from photons and should not be included in all hadron spectra.

The size of the circle or square is enlarged for visibility and does not reflect determination precision of particle emission angles. As shown in previous sections in this chapter, the accuracy of emission angle determination in the emulsion chamber is

$$\tan \Delta\theta_{\text{LAB}} \leq 0.0001$$

and

$$\tan \Delta\phi \leq 0.0001.$$

The resolution of emission angle is better than 0.005 degree. As an example we show one of EMU05 event #4750 in Figure 3.17. The histogram shown on the right-hand side is a distribution of all particles in azimuth bins. The width of the bin is set to 10 degrees in this and all pseudo-rapidity azimuth distribution plots.

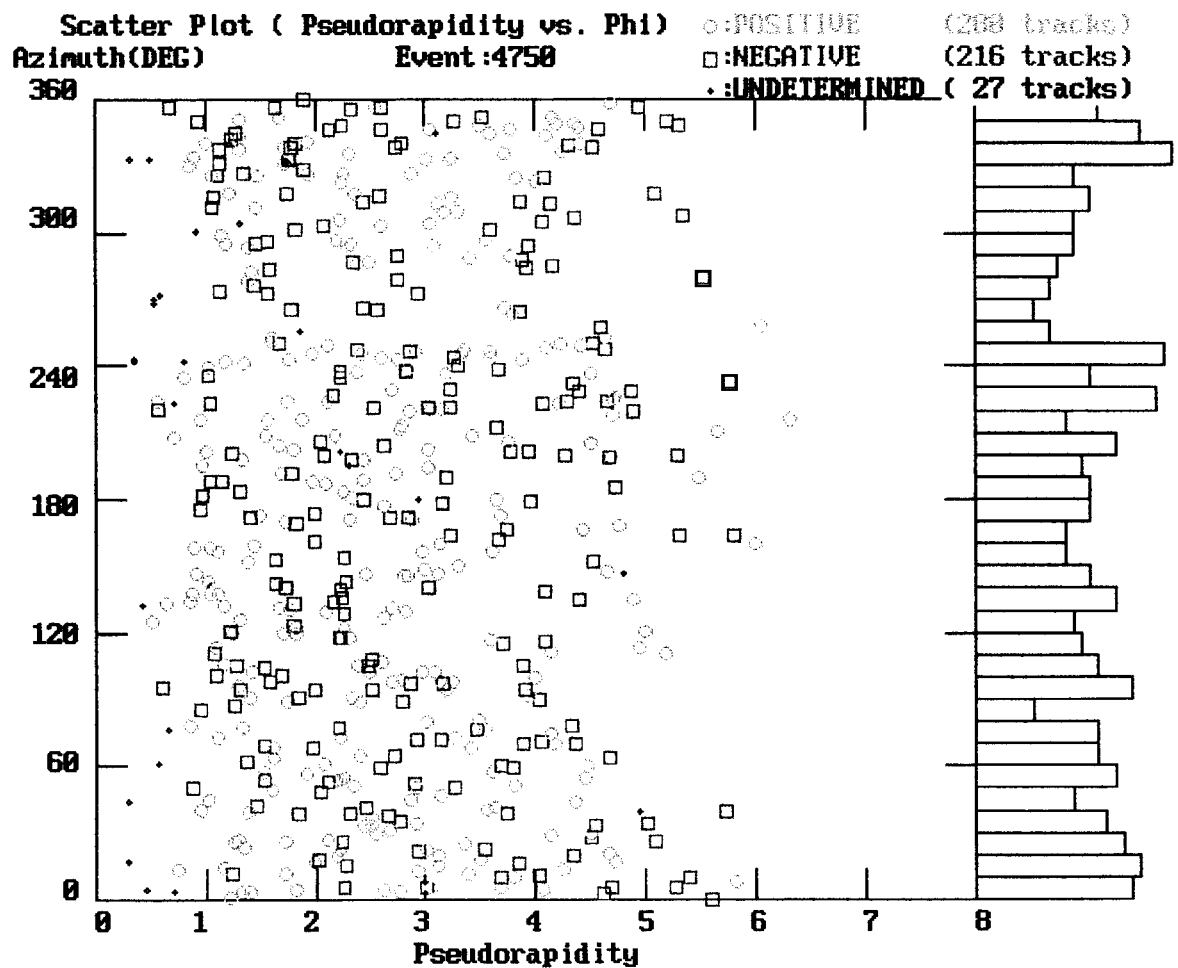


Figure 3.17 Pseudorapidity – azimuth angle distribution and all particle histogram in azimuth angle (EMU05 event 4750).

3.5.2 Pseudorapidity Distributions (event by event)

Pseudorapidity distributions ($dN/d\eta$) of all events are obtained for EMU05, EMU09, and EMU16 events individually. The $dN/d\eta$ distribution is used to characterize the event profile in high energy nuclear collisions since $dN/d\eta$ distribution is known to be a rather constant fraction of the total collision energy.

Pseudorapidity distributions for individual events of EMU05, EMU09, and EMU16 are shown in APPENDIX B (Figures B.1 through B.42) due to the volume of plots. Shown in Figure 3.18 below is a semi-inclusive pseudorapidity distribution of all sulfur events of EMU05 and EMU09. The values shown in the upper right corner of the plot are the average number of particles calculated from the pseudorapidity range $2 < \eta < 4$. dN_a/dY is for all particles, dN_p/dY is for positively charged particles, and dN_n/dY is for negatively charged particles. Y stands for pseudorapidity η in this plot and all the plots in APPENDIX B. As in the pseudorapidity – azimuth distribution plots, particles of which the charge signs were not determined because of large errors in curvature fitting, insufficient data points are not included. An “impact parameter” cut is also applied in semi-inclusive data and all individual data shown in APPENDIX B.

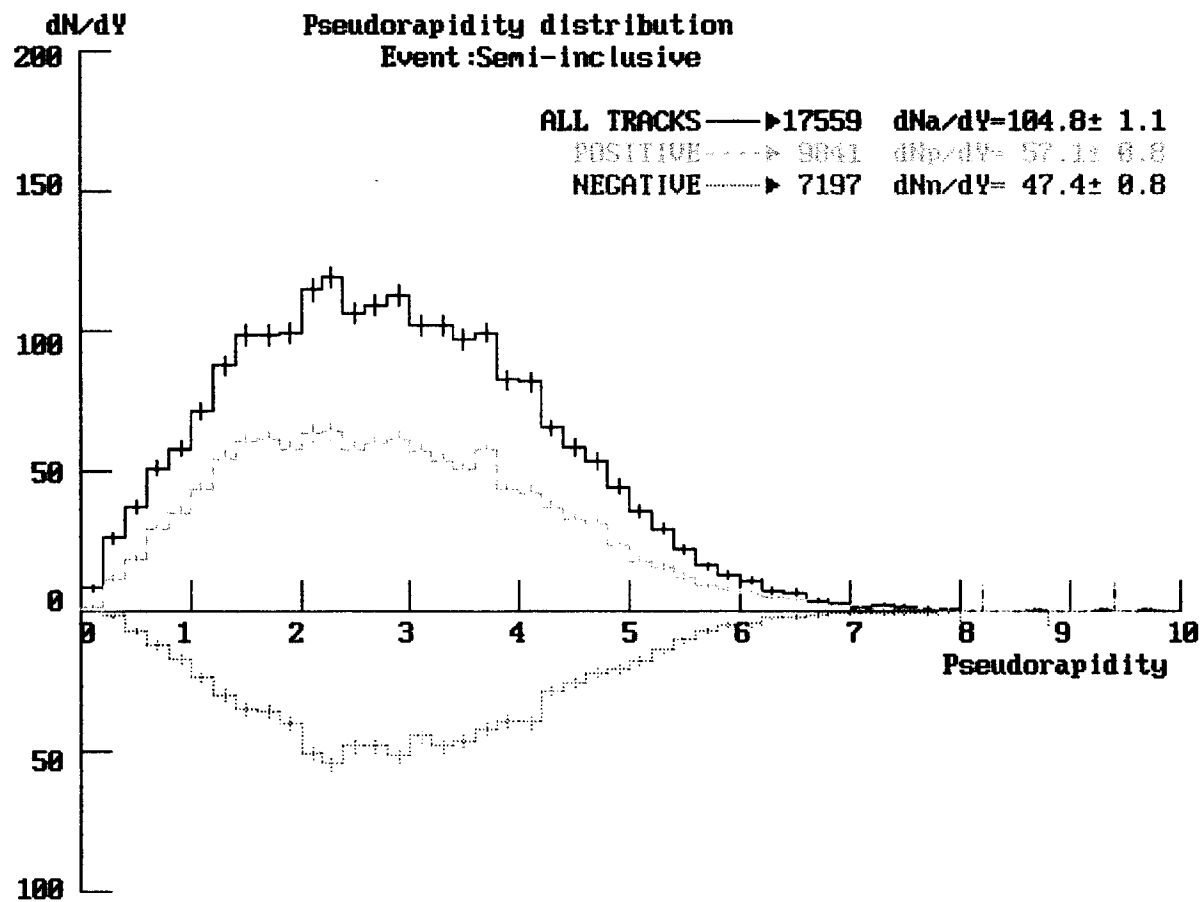


Figure 3.18 Semi-inclusive pseudorapidity distribution for all 41 sulfur events of EMU05 and EMU09.

3.5.3 Transverse Momentum Distribution (event by event)

Transverse momentum distributions of all events measured in EMU05, EMU09, and EMU16 are presented in APPENDIX C (Figures C.1 through C.42). As in the previous two plots, possible electron contamination was eliminated from the data. All transverse momentum distributions are well fit by a single exponential function, which is expressed as

$$dN/dPt/Pt \propto \exp(-Pt/P_0),$$

where P_t is transverse momentum and P_0 is the slope value, and they are consistent with earlier EMU05 data. The parameter fit was done by the maximum likelihood method in the pseudorapidity range $2 < \eta < 4$ and the transverse momentum range $0 < P_t < 1.2 \text{ GeV}/c$. Small transverse momentum enhancement was reported by NA34 earlier [72]. Our data do not show any significant over population of small P_t . Shown in Figure 3.19 is the transverse momentum distribution for all sulfur events of EMU05 and EMU09. In all transverse momentum distribution plots, in order to enhance the visibility of data for the three different charges in one plot, all particle data is multiplied by a factor of 10 and negative charge particle data is divided by a factor of 10. Since the plot is in log scale, such multiplication shifts data by a factor of 1 up (all) or down (negative).

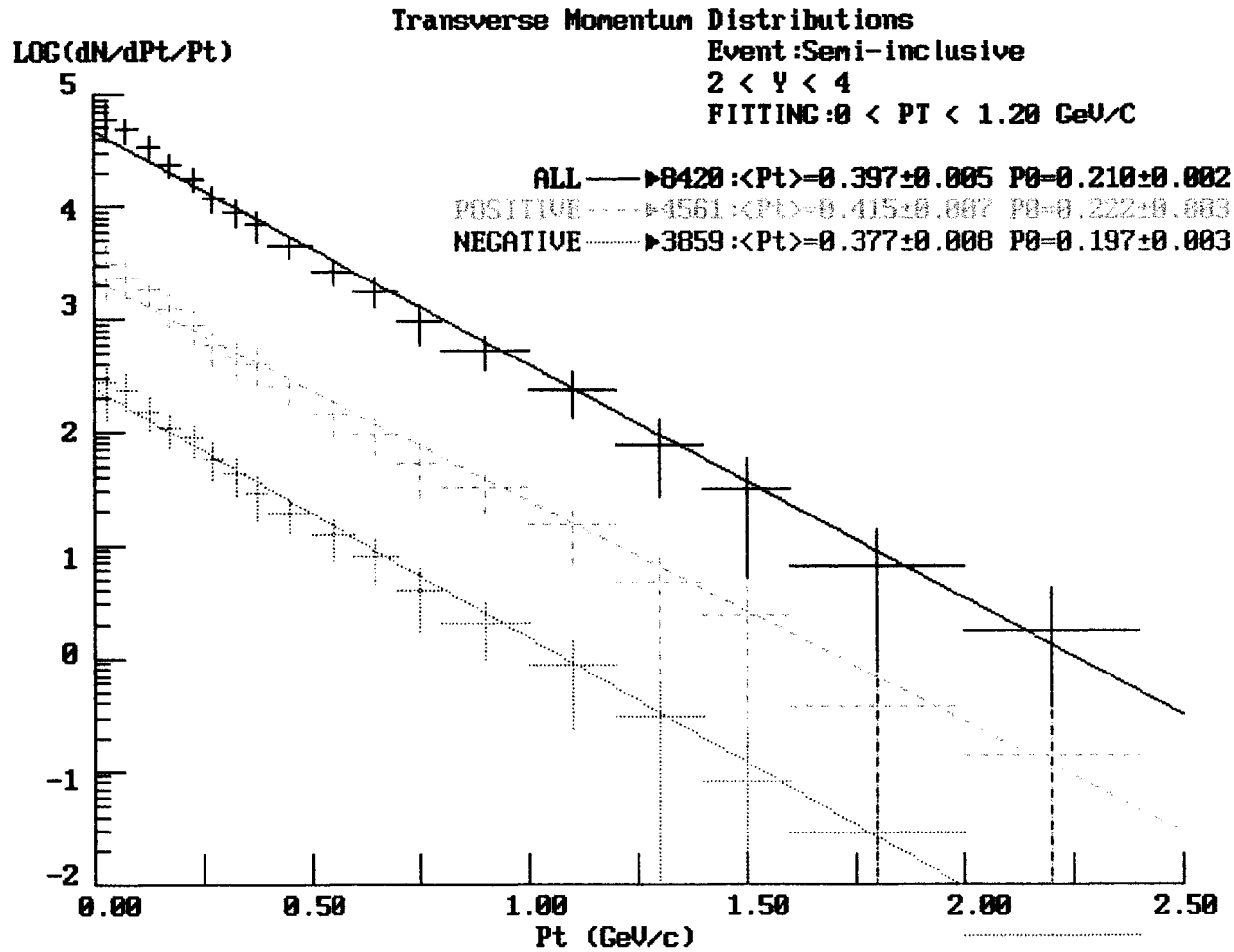


Figure 3.19 Transverse momentum distribution for all 41 sulfur events of EMU05 and EMU09.

3.5.4 Two Particle Correlations

The precise determination of individual particle momentum and charge-sign also makes it possible to evaluate the two particle correlation function C_2 for the estimate of the source size as reviewed in Section 2.4.3. Combined with an estimate of the energy density, we may be able to estimate the total energy deposited in a small region of space and time, which may give an estimate of an upper limit of number of pions emitted from this energetic source. Such information should assist in the estimate of the upper limit of the periodic isospin cluster signal in the canonical Fourier analysis. However, the data were not utilized for the source size estimate or energy density estimate in this dissertation. Since the EMU05, EMU09, and EMU16 data provide necessary physical quantities for these estimates, we shall leave them for the second phase of data analysis.

3.5.5 Multiparticle Charge-Sign Clusters

It is the main objective of this dissertation to quantitatively and objectively evaluate the degree of charge-sign clusters and the periodicity of them, if they exist, utilizing the precise determination of emission angles and charge-signs as presented in Sections 3.1 through 3.3. Since our emission angle and charge-sign data are obtained particle by particle, we can examine all charged particles in arbitrary bin size and in all phase space. (We are not limited by detectors finite granularity or limited acceptance.)

As already stated in the theoretical part of this thesis, one theory in fact suggests that periodic charge-sign clusters may be the signal of decay of a region of disoriented chiral condensate (DCC) which may be formed in high energy heavy ion collisions. A proof of the existence of such a signal beyond statistical coincidence may provide evidence for the DCC formation. However, the current theory does not give quantitative details of how such clusters should exhibit themselves in nature. The statistical examination of all-particle spectra that the EMU05, EMU09, and EMU16 data provides is hoped to provide some exploration of the possibility of the DCC formation. In the following chapters, we present how we performed the canonical Fourier analysis on the EMU05, EMU09, and EMU16 data in search of a periodic isospin cluster signal. We discuss the definition and capability of the analysis and our first result in the following chapter.

4. METHOD OF CANONICAL FOURIER ANALYSIS

The canonical Fourier analysis, as described below, tests the regularity of the appearance of clusters for a quantitative characterization of a possible phase correlation, if there are any periodic charge-sign clusters [73].

§4.1 Definition of Canonical Fourier Analysis

We first define the canonical Fourier analysis that is performed for the search of DCC clusters. Unlike the previous two EMU05 cluster analyses, this new method treats positive and negative charge distributions separately, which removes the constraint of the non-existence of a positive cluster over a negative cluster (or vice versa) in pseudorapidity – azimuth angle ($\eta - \phi$) space.

A ring segment defined by rapidity is divided into n_{bin} bins ($n_{\text{bin}} = 360 / \Delta\phi$) for the multiplicity distributions of + and – signs N_j^\pm . From the distribution of – signs, a discrete Fourier cosine component with a phase parameter δ_S is defined as

$$a_k^- = \frac{2}{n_{\text{bin}}} \sum_{j=0}^{n_{\text{bin}}-1} N_j^- \cos\left(\frac{2\pi k j}{n_{\text{bin}}} + \delta_S\right),$$

where k is a wave number, and

$$k = 0, 0.1, 0.2, \dots, \frac{n_{\text{bin}}}{2}.$$

The phase parameter δ_S is determined so that the highest peak of $|a_k^-|$ is maximized when δ_S is varied from 0 to 2π .

A discrete Fourier sine component is taken for + signs as

$$b_k^+ = \frac{2}{n_{\text{bin}}} \sum_{j=0}^{n_{\text{bin}}-1} N_j^+ \sin\left(\frac{2\pi k j}{n_{\text{bin}}} + \delta_S + \frac{\pi}{m_S k}\right),$$

where k is a wave number, and

$$k = 0.1, 0.2, \dots, \frac{n_{\text{bin}}}{2}.$$

The ring segment is a region in $\eta - \phi$ space that is between two concentric circles around the beam axis. The diameter of an outer circle corresponds to a smaller η value by

definition of η . The parameter m is determined so that the highest peak of $|b_k^+|$ is maximized. The phase shift parameter δ_S is already determined when the maximum of $|a_k^-|$ is sought. The only degree of freedom that b_k^+ has is the parameter we call the wave shift parameter m_S . The wave shift parameter m_S is introduced as a measure of correlation between the two dominant sinusoidal waves which represent positive and negative clusters when two waves share the same wave length, m_S takes a value of $1, 2, \dots, 8$, and ∞ , where ∞ means there is no phase shift due to the wave shift parameter m_S . The width and diameter of the ring segment must be determined to extract the cluster signal the most effectively. Thus all the parameters δ_S , m_S and the spectra a_k^- , b_k^+ can be uniquely determined without any bias to characterize possible cluster signals.

§4.2 Definition of Normalized Lomb Periodogram

In order to determine the pseudorapidity range (ring segment) and the phase shift parameter δ_S that give the maximum signal, a normalized Lomb periodogram (NLP) is used. The Normalized Lomb Periodogram [74] has been developed in astrophysics for the effective spectral analysis of time series [4]. We have a data set of

$$\xi_i = \xi(t_i) \text{ for } i = 1, 2, \dots, N_T$$

with

$$\bar{\xi} \equiv \frac{1}{N_T} \sum_{i=1}^{N_T} \xi_i$$

and

$$\sigma_V^2 \equiv \frac{1}{N_T - 1} \sum_{i=1}^{N_T} (\xi_i - \bar{\xi})^2.$$

The Normalized Lomb periodogram $P_N(\omega)$ of an angular frequency ω is defined as

$$P_N(\omega) \equiv \frac{1}{2\sigma_V^2} \left\{ \frac{\left[\sum_{j=1}^{N_T} (\xi_j - \bar{\xi}) \cos \omega(t_j - \tau_c) \right]^2}{\sum_{j=1}^{N_T} \cos^2 \omega(t_j - \tau_c)} + \frac{\left[\sum_{j=1}^{N_T} (\xi_j - \bar{\xi}) \sin \omega(t_j - \tau_c) \right]^2}{\sum_{j=1}^{N_T} \sin^2 \omega(t_j - \tau_c)} \right\},$$

where $\omega > 0$.

The constant τ_c is defined by the relation:

$$\tan(2\omega\tau_c) = \frac{\sum_{j=1}^{N_T} \sin 2\omega t_j}{\sum_{j=1}^{N_T} \cos 2\omega t_j}.$$

The statistical meaning of the periodogram is the following [4][74]. When the normalized Lomb periodogram $P_N(\omega)$ gives some value at some frequency ω_0 , it is exponentially unlikely that a periodic signal having frequency ω_0 is due to a random noise coincidence. That is, the probability of a random coincidence of such a periodic signal with ω_0 frequency is given by

$$\left\{ 1 - \left(1 - \exp[-P_N(\omega_0)] \right) \right\}^{N_f},$$

where N_f is the number of frequencies scanned.

Therefore one can set a threshold value of the periodogram and detect periodic signals with the set confidence level. We adopt a normalized Lomb periodogram to seek any significant periodic signals in negative and positive charge distributions.

§4.3 Application of Canonical Fourier Analyses to EMU05, EMU09, and EMU16 Data

The normalized Lomb periodogram discussed in the previous section can be used as a threshold against the random noise coincidence. Our current noise probability threshold is set to 5%. That is, if a periodic signal is found above this threshold value, we can be 95% certain that such a signal is not due to some random coincidence. We then seek an optimal set of parameters such as the pseudorapidity range and phase shift parameters which should give the maximum value of the Fourier cosine and sine

component discussed in Section 4.1. The details of the parameter selection are as follows.

1. Define a ring segment by two pseudorapidity values, η_{high} and η_{low} , satisfying the following requirements.
 - i) The minimum number of either negative or positive tracks is 90.
 - ii) The maximum number of tracks is 350.
 - iii) The step size of the pseudorapidity is fixed to 0.15 regardless of how populated the selected ring segment is.
2. Take a number distribution for both charges, N_j^- and N_j^+ . The bin size is set to 10 degrees ($j = 1, 2, \dots, 36$). (The origin of ϕ is shifted by 1.5 degree after each run of periodogram. The azimuth angle shift ϕ_{LAB} from the origin replaces the phase shift parameter δ_S defined in Section 4.1.)
3. Apply periodogram method to N_j^- and N_j^+ .
4. Repeat steps 2 and 3 240 times shifting the origin of ϕ by 1.5 degree to rotate the origin of ϕ by 360 degrees. Pick a parameter set, η_{high} , η_{low} , and ϕ_{LAB} that give the maximum NLP value. If random coincidence probabilities for both positive and negative charge distributions are less than 5%, store the parameter set as a signal candidate for the event.
5. Repeat step 1, 2, 3, and 4 until the entire η - ϕ space is covered.
6. Select independent rings among candidates by imposing the following conditions.
 - i) The ring segment that gives the minimum of $\sqrt{(P_{r-})^2 + (P_{r+})^2}$ is the primary candidate, where $P_{r-/+}$ denotes random noise coincidence probabilities for negative/positive charge distributions.
 - ii) The overlap of the two rings does not exceed 1.0 in η regardless of the number of particles contained in the overlapped region.

7. Run the canonical Fourier analysis for each event with the selected set(s) of parameters.

The above method detects sinusoidal signals of charge distributions in η - ϕ space with 95% confidence if they exist. And the determined set of parameters should give the optimal set of wave numbers with which a single wave length sinusoidal wave can well fit to the original charge distribution for negative and positive signs independently.

Furthermore in order to examine the possibility of DCC formation in heavy ion collisions, we must examine how unlikely it is to find periodic signals in events that consist of the incoherent emission of particles. In this dissertation, events of incoherent emission of secondary particles are generated by randomizing the charge distribution of observed events. If periodic signal detection does not occur in randomly generated events by the same method, we find that our high energy heavy ion collision events may contain particles created by some microscopic mechanism of the nuclear collision – possibly DCC. On the other hand, if periodic signals are often found in randomly generated events, the charge-sign clustering we find in our data may well have incoherent origins. Therefore, the frequency of the occurrence of such events among randomly generated events has to be examined. The randomly generated events are simulated by fixing the original pseudorapidity determined for each particle η_i ($i = 1, 2, \dots, N_{ch}$, where N_{ch} is the multiplicity of negative or positive charge in one event), and redistributing all particles in the ϕ -direction such that the probability of one particle falling into the j -th bin N_j (the number distribution in ϕ) is equal for all j 's ($1 \leq j \leq 36$).

In order to demonstrate the periodic signal detection efficiency, an artificial ring segment having a pseudorapidity range from 2.082 to 2.805 was created. Figure 4.1 shows the target diagram for this ring segment of the purely clustering artificial event #1111. This artificial ring segment contains 120 negative charges in 6 pure clusters and 96 positive charges in 8 pure clusters. All the clusters are aligned in the phi direction with equal spacing. One negative cluster contains 20 ($=120/6$) particles and one positive cluster contains 12 ($=96/8$) particles. Within one cluster of diameter 0.735 ($= 2.805 - 2.802$), particles are distributed randomly. Numbers listed in the upper left corner of Figure 4.1 are

- Event: 1111 – event number (For this artificial event 1111 is assigned)
- min: 2.082 – pseudorapidity of outer ring
- max: 2.805 – pseudorapidity of inner ring
- neg: 120 – total number of negative charges in the ring segment (closed circle)

pos: 96 – total number of positive charges in the ring segment (open circle)

The phase shift is done by shifting the origin of azimuth angle by ϕ_{LAB} listed in the upper right corner ($\phi_{\text{LAB}}=97.5$ deg).

We applied our cluster analysis method to the ring segment and successfully extracted periodic signals at frequency 6 for a negative charge and 8 for a positive charge distributions. Figure 4.2 is a reproduction of this artificial event by the Fourier coefficients. The vertical axis is the amplitude of the Fourier coefficient. The upper plot is for the negative charge distribution and the lower plot is for the positive charge distribution. Thin dark vertical lines at 5, 15, ..., 375 degrees in ϕ are a modified histogram of the original charge distribution. This thin line is modified from the original charge distribution such that the amplitude 0 corresponds to $\langle N_j^\pm \rangle$ (average number of particles in n_{bin} bins. That means that the first component of the Fourier cosine series for the negative charge a_0^- is always set to zero. The equation written over the plot is the dominant cosine or sine wave which represents the charge distribution the best, which is shown with a shaded curve over the modified histogram. The equation written over the lower plot has an extra term. That is the wave shift parameter m_s we introduced above. For this demonstration m_s was determined to be 2. However as we mentioned earlier, the wave shift parameter m_s was introduced as a correlation measure of the cosine and sine function when the dominant frequencies are similar. Although the wave shift parameter m_s was determined, m_s loses its significance when two dominant frequencies are different. The wave number parameter dependency of the Fourier sine coefficient was insignificant in this demonstration.

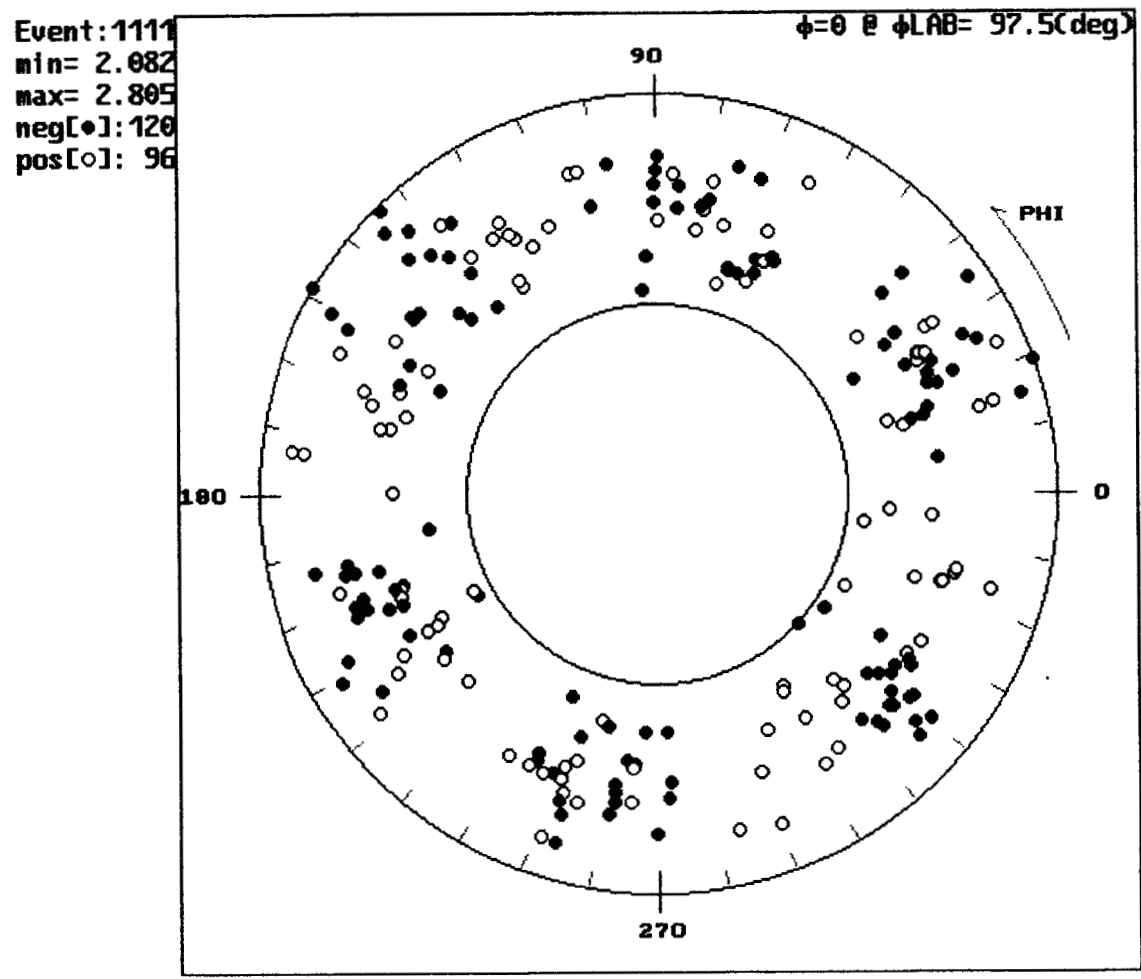
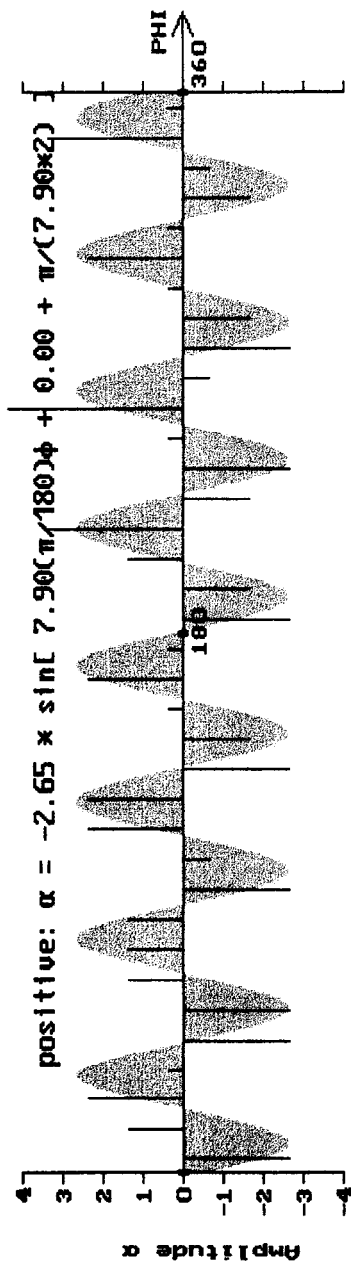
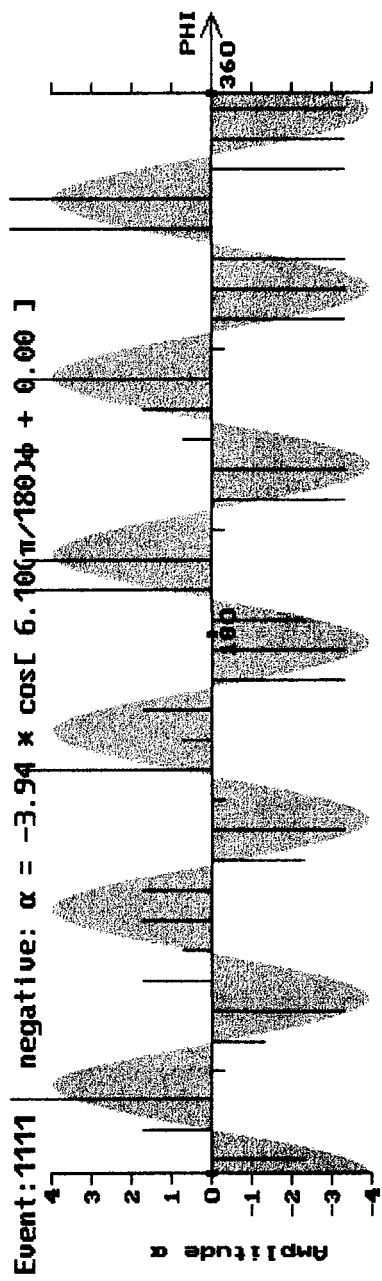


Figure 4.1 Target diagram of artificial event #1111 containing pure clusters.



5. RESULTS AND EVALUATION

All 41 sulfur (200 GeV/nucleon) + lead events and 1 lead (158 GeV/nucleon) + lead event were examined by the method described in the previous chapter. We present the results of the canonical Fourier analysis and evaluate the method and the results.

§5.1 Results of Canonical Fourier Analysis

Table 5.1 below shows the result of the normalized Lomb periodogram of all data including the results of the same analysis on the randomly generated 300 events. The meaning of each column is

1. Experiment: experiment name
2. Event: event name – four digits
3. Eta-high: higher bound of ring segment in pseudorapidity (inner ring)
4. Eta-low: lower bound of ring segment in pseudorapidity (outer ring)
5. Phi shift: phase shift in phi (degree)
6. K^- : wave number of the sinusoidal wave which most well represents the negative charge distribution
7. $Pr\ max^-$: probability of the signal at k^- to be due to statistical noise
8. Nch^- : number of negative-charged particles in the ring segment
9. K^+ : wave number of sinusoidal wave which most well represents the positive charge distribution
10. $Pr\ max^+$: probability of the signal at k^+ to be due to statistical noise
11. Nch^+ : number of positive-charged particles in the ring segment
12. Random run: number of periodogram runs with randomly produced charge distribution

13. $Pr < 0.05$: number of randomly produced events found to have a noise probability less than 5% at any wave number

Events showing numbers in columns 3 through 11 are the ones that showed signals with noise probability less than 5% in the actual charge distributions. Columns 3 through 11 are left blank if the event does not contain such a periodic signal in the true charge distributions. We notice that the number of negative charged particles ($N_{ch -}$) and the number of positive charge particles ($N_{ch +}$) are often different in the same ring segment of the same event – almost consistently the number of positive charge particles is larger than that of negative charge particles except in the event #0324, #5426, and #9876 of EMU09. Electric charge conservation is exact in strong interactions. So the positive charge excess coming from both projectile and target nuclei always exists. This is reflected in almost all the eta-phi space. Local charge distribution statistically fluctuates even in the completely incoherent case of particle emission. Noting this nature, we consider that the observed positive charge excess in one ring segment is consistent within the statistical fluctuation of the initial positive-charge excess.

Table 5.1 Result of normalized Lomb periodogram runs for all events of EMU05, EMU09, and EMU16.

Experiment	Event	Eta-high	Eta-low	Phi shift	K -	Pr max -	Nch -	K +	Pr max +	Nch +	Random run	Pr<0.05
EMU05	0385	5.739	2.502	286.5	4	0.03306	108	9	0.04721	117	300	202
EMU05	0396										300	205
EMU05	0704										300	197
EMU05	0757										300	0
EMU05	2764										244	178
EMU05	3141	4.027	1.867	48.0	6	0.00608	103	16	0.01977	143	300	172
EMU05	3245										300	205
EMU05	3542	2.957	0.274	285.0	8	0.01990	104	16	0.01783	169	300	206
EMU05	3745	5.321	1.089	267.0	16	0.03973	134	3	0.04347	164	300	152
EMU05	4048										300	178
EMU05	4141										300	188
EMU05	4142										300	207
EMU05	4243										300	0
EMU05	4251	3.918	1.272	127.5	12	0.02396	109	6	0.02041	139	300	170

Table 5.1 (Continued)

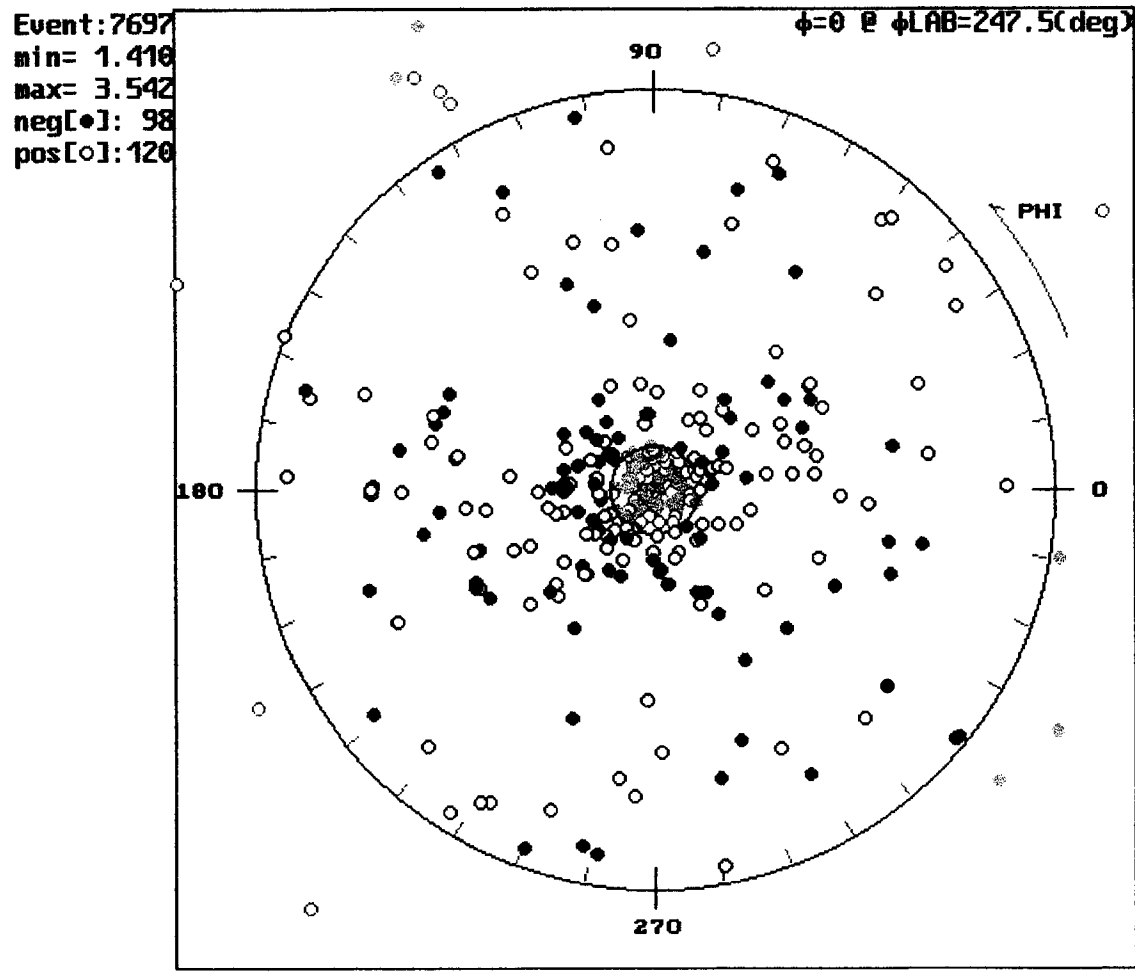
Experiment	Event	Eta-high	Eta-low	Phi shift	K -	Pr max -	Nch -	K +	Pr max +	Nch +	Random run	Pr<0.05
EMU05	4537										300	162
EMU05	4556										300	170
EMU05	4750										300	193
EMU05	5024	6.555	2.453	147.0	16	0.02024	150	5	0.02366	164	300	217
EMU05	5882										300	203
EMU05	6106	5.885	2.477	58.5	13	0.04617	104	11	0.01343	126	300	212
EMU05	6115	5.923	2.605	120.0	17	0.03108	109	15	0.02829	137	300	212
EMU05	6116	6.256	2.248	232.5	3	0.03240	139	5	0.02335	173	300	193
EMU05	6500	5.986	2.630	337.5	17	0.01745	119	15	0.01286	127	300	202
EMU05	6621	3.925	2.068	82.5	13	0.01319	98	6	0.02769	110	300	205
EMU05	6677	5.234	2.537	187.5	16	0.03170	107	15	0.04979	126	300	217
EMU05	6690	5.858	2.623	199.5	12	0.02303	91	17	0.01769	130	300	161
EMU05	6796	3.370	0.257	262.5	2	0.03779	137	6	0.03518	183	300	222
EMU05	6807										300	211

Experiment	Event	Eta-high	Eta-low	Phi shift	K -	Pr max -	Nch -	K +	Pr max +	Nch +	Random run	Pr<0.05
EMU05	7188										300	164
EMU05	7697	3.542	1.410	247.5	15	0.00886	98	2	0.00643	120	300	190
EMU09	0324	4.491	2.238	304.5	6	0.02063	141	6	0.02268	121	300	202
EMU09	4444										300	183
EMU09	4895										300	171
EMU09	5025										300	158
EMU09	5040										300	173
EMU09	5338	6.625	1.875	159.0	3	0.04908	139	11	0.01396	184	300	165
EMU09	5426	5.217	2.159	132.0	2	0.02818	96	6	0.01549	94	300	105
EMU09	5538										300	147
EMU09	5684										300	171
EMU09	5986										300	0
EMU09	9876	4.348	1.566	87.0	12	0.04730	96	18	0.04173	91	300	143
EMU16	160i	5.620	4.406	126.0	16	0.04179	100	7	0.04350	151	300	256

Event #7697 of EMU05 particularly shows a very low probability of random noise coincidence level for periodic signals of frequency 15 and 2 for negative and positive charge distributions respectively. It is confirmed by the reproduction of the ring segment ($1.410 \leq \eta \leq 3.542$) that the dominant frequencies are about 2 and 15 as shown in Figures 5.1 and 5.2. However, 190 of 300 randomly generated events from event #7697 also contained a periodic charge-sign distribution with arbitrary wave numbers for both negative and positive charge distributions. Therefore within the limit of capability of our method and the number of available data, it seems that periodic clustering may occur in the multiparticle production of an incoherent source in heavy ion collisions.

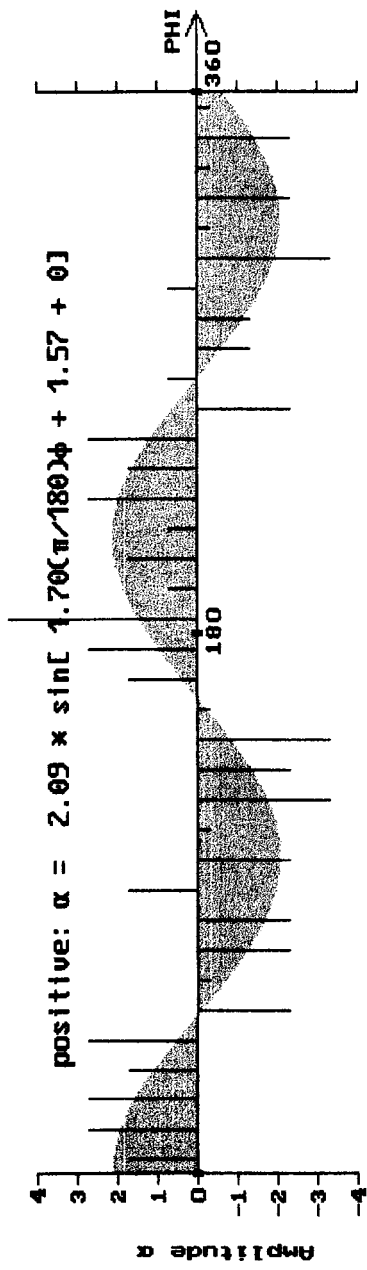
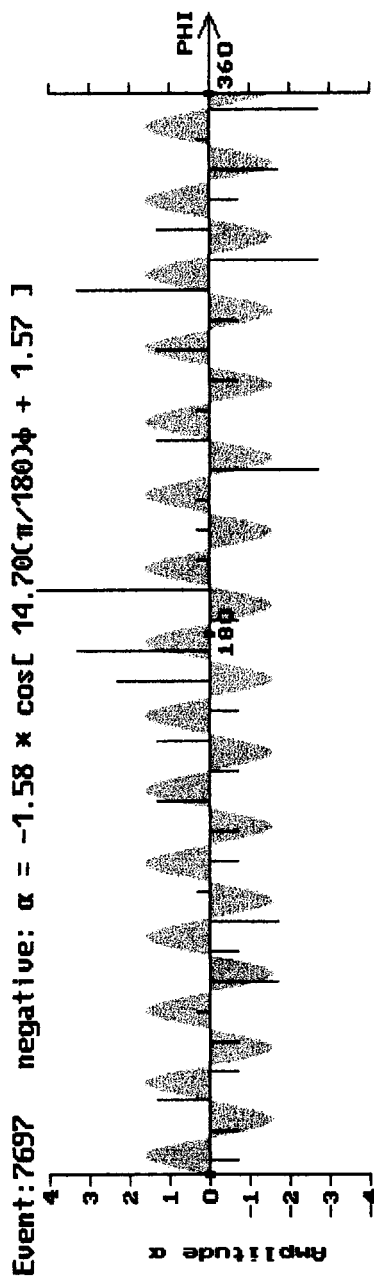
Target diagrams and reproduction of the charge distributions using dominant Fourier coefficients for all events with at least one pair of periodic signals found in the original charge distributions are shown in APPENDIX D in Figures D.1 through D.40. The meaning of numbers shown in the figures is the same as what we already explained in the previous chapter for the artificially generated event #1111.

The wave shift parameter m_s shown in the ring segment reproduction plot in APPENDIX D as the last term of argument of sine function (even numbered figures). However as indicated in Chapter 4, the wave shift parameter was intended to probe the phase correlation between negative and positive charge distributions when the dominant frequency is close. That is, when the numbers in $K -$ and $K +$ columns are comparable. As Table 5.1 shows, the two frequencies are often different. There are some correspondences, but the number of events is not large enough for a correlation study.



75

Figure 5.1 Target diagram of the ring segment which has periodic signals (event #7697, EMU05).



§5.2 Evaluation

In an ideal case, to prove the existence of periodic clusters, one would expect a clear signal (with 95% confidence level or higher) in the true events and no such signals in randomly generated events. Such high statistical confidence or more is necessary to prove the existence of any periodic charge-sign clusters of negatively and positively charged particle distributions. To disprove the existence of periodic clusters, one would expect no such random-oriented pseudo-signals for true events. What we found in the canonical Fourier analysis was that 20 of 42 events had some periodic signals in observed charge distributions $\sim 50\%$ of all the fully analyzed events. On the other hand, more than 60% (in average) of the randomly generated events showed such signals. Thus, the analysis indicated either the sensitivity of the analysis method is too low, or there are no significant signals of clusters in the experimentally measured data set.

Two extreme cases should be considered to evaluate the sensitivity of the canonical Fourier analysis to extract the signal of periodic charge-sign clusters. One case we consider is events having purely periodic charge-sign clusters. The other is events with purely random charge-sign distributions. The latter was generated by Monte Carlo method for the randomized events, where all negative and positive charges were completely randomly redistributed in eta-phi space.

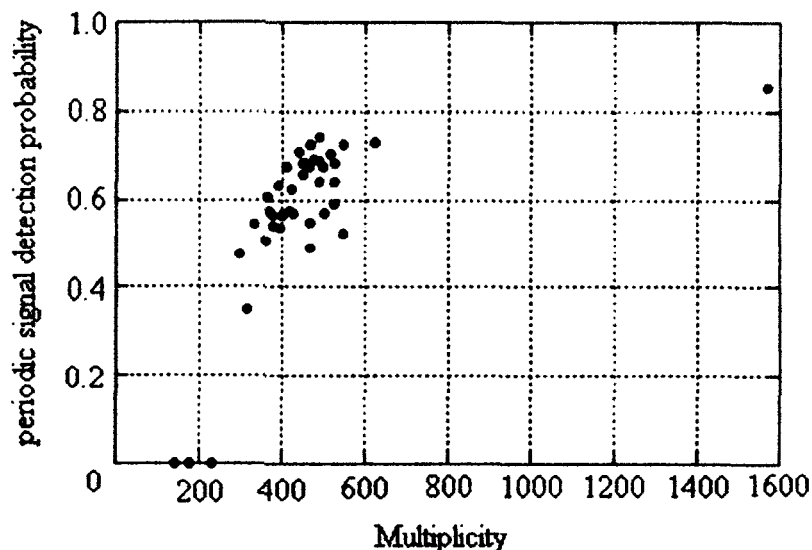


Figure 5.3 Multiplicity vs. periodic signal detection probability.

Figure 5.3 shows the correlation between event total multiplicity and the probability of finding any periodic cluster signal in randomly generated events. Each dot

represents the probability of finding at least one periodic signal in both randomly generated negative and positive charge distributions. There is a vertical cutoff line around the total multiplicity = 180, because we require both negative and positive charge multiplicity to be larger or equal to 90 for valid signal detection. The plot exhibits some characteristics of the cumulative distribution function. That is,

- 1) The probability of finding a periodic signal in random events is larger when the event total multiplicity is larger.
- 2) The probability of finding a periodic signal in random events monotonically increases as the multiplicity increases. (One would find some periodic signal among infinite number of particles.)

One needs to carefully select the minimum cutoff value, for the probability of finding a periodic signal in a distribution of charge multiplicity of one is clearly 1 at the wave number of 0.5.

The other extreme case is an event containing purely periodic clusters. Event #1111 shown in Figure 4.1 was generated also to evaluate the probability of finding at least one periodic cluster signal when the artificial pure cluster event is randomized (6 negative charge clusters each containing 20 particles and 8 positive charge clusters each containing 12 particles). We found at least 1 periodic signal in 30% of the randomly generated events from this originally pure artificial event.

Although the origins of the events in the two extreme cases were different (true events vs. artificially created event), the randomization process was done in exactly the same manner and the randomization is believed to be complete. We must examine this situation further in terms of the multiplicity dependence of the probability of finding at least one periodic signal in randomly regenerated events. It is expected to follow the statistically characteristic curve. In this canonical Fourier analysis with the current set of the criteria, we can only expect to prove the existence of at least one periodic charge-sign clustering signal beyond statistical coincidence only 40% of the time.

§5.3 Prospect

First, our canonical Fourier analysis method is apparently accepting more noise than desired for clean signal detection. We should raise the confidence level of Lomb's periodogram from our currently set value of 95% to a higher value so that no or very few randomly re-generated events should show periodic cluster signals. On the other hand we already learned that the best fit of periodic signals to the true event data was that of the

EMU05, event #7697, with the periodic signal detection confidence level of higher than 99% for both negative and positive charged particle distributions in the pseudorapidity range, $1.410 \leq \eta \leq 3.542$. We can investigate the probability of detecting a periodic cluster signal with such a high level of confidence in randomly re-generated events. We also learned that if we set our confidence threshold to be set as high as 99%, all other events, and those random-generated events, would not exhibit any signature of existence of periodic cluster signals. We need to investigate the relationship of noise detection probability vs. multiplicity more thoroughly to set an optimized confidence threshold value for more effective and reliable signal detection.

Nonetheless, the presently-available data set has one significant candidate, event #7697 of EMU05. The particularly impressive event, #4750, of which the run-test and G-test already indicated that the statistical significance of clustering is not beyond random coincidence, did not exhibit any significant periodic signals in canonical Fourier analysis. This statistic (one event) is obviously too insufficient to draw any meaningful conclusions for the existence of Disoriented Chiral Condensate. We tried in this dissertation to extract more events with cluster signals from the existing data including event #4750 by using the canonical Fourier analysis. The results of the canonical Fourier analysis confirmed the G-test/run-test results, and could not increase the number of meaningful candidate events. Unless an increase of statistics by orders of magnitude becomes available from further experiments, events #4750 and #7697 should remain as episodic events. What we have achieved by the canonical Fourier analysis is that the DCC signals can be statistically extractable and testable in a quantitative way using a normalized Lomb periodogram.

Next, possible improvement may be accomplished by further elimination of electron pairs in the all-track data. They are converted in the residual target lead from photons as decay products of neutral pions, which potentially destroy the high statistical significance of isospin clusters so long as the measurements remain to provide the charge-sign data alone. We can achieve the non-statistical elimination of electron pairs by selecting events with a smaller residual target following the event. The present data have not completely eliminated electron pairs, although the achieved level of elimination was much higher than most of the other experiments. The elimination of electron pair candidates should be performed on data before searching for periodic cluster signals in our data. It would also be useful to simulate an acceptable contamination level by creating a pure periodic cluster event artificially and slowly adding randomly distributed artificial background noise and investigating how much noise would make the pure signal undetectable in the analysis. One must be careful to control the multiplicity of the event

during this examination since as the plot in Figure 5.3 indicated, signal detection probability increases as the multiplicity increases. However if we are able to establish the upper limit of the acceptable contamination level for a given multiplicity, we may be able to optimize the maximum number of particles in one ring segment, which is currently set to 350. We will leave these further investigations and optimizations for future analysis with increased statistics.

CONCLUSION

Central collision events of CERN EMU05, EMU09, and EMU16 were fully measured and analyzed for the search of the periodic signal of charge-sign clusters in secondary particle distributions.

The method of canonical Fourier analysis was defined and performed on charge-sign distributions of all 41 S+Pb and 1 Pb + Pb central events. The canonical Fourier analysis showed the existence of signals of periodic negative and positive charge clusters in half of the 42 events with 95% confidence level. However the probability of detecting such a periodic charge-sign pattern in randomly generated events is more than 60% at the same confidence level. The canonical Fourier analysis was also applied to a purely artificial periodic cluster event in order to investigate the validity of the analysis and randomness of the simulated events. This artificial event, #1111, was also randomized and analyzed by the same method. About 30% of the randomized events from the artificial event #1111 also included significant periodic signals. It was found that the probability of finding at least one periodic signal in a given pseudorapidity ring segment in randomly regenerated events strongly depends on the total event multiplicity. At the highest multiplicity level of 200GeV/nucleon S + Pb central collisions (more than 500), the probability of detecting periodic signal in randomly generated events, which should not contain such signal, was found to be about 60%. This noise detection probability was set too high for clear signal detection. Therefore we conclude that the possibility of the existence of periodic charge-sign distribution in 200GeV/nucleon S + Pb central collisions remains as only one event EMU05 #7697. Excepting this event, the majority of the experimental data is consistent with statistical coincidence level, if the cluster finding confidence level is set at 95%. The upper limit of probability of detecting periodic signal in observed charge distributions in true events and not detecting any such periodic signal in randomly regenerated events is at most 40% in the multiplicity range of central events of S (200GeV/nucleon) + Pb events.

One possible scenario of chiral phase transition from DCC to normal vacuum in high-energy heavy-ion collisions suggests that periodic isospin (charge-sign) clusters like our particular event #7697 suggested. The sensitivity of the analysis for the existence of

periodic charge-sign clusters leaves room for future improvement, and our new objective method of canonical Fourier analysis showed no positive evidence of the existence of periodic isospin clustering for the rest of the events (41 events of 200 GeV/nucleon S + Pb and 1 event of 158 GeV/nucleon Pb + Pb central collisions) measured in EMU05, EMU09, and EMU16 experiments.

REFERENCES

- [1] T.H. Burnett, et al., Phys. Rev. Lett. 51, 1010 (1983); W.V. Jones, B. Wosiek, and Y. Takahashi, Ann. Rev Nucl. Part. Sci. 37, 71 (1987)
- [2] Y. Takahashi, et al., Nucl. Phys. A525, 591c (1991)
- [3] A. Iyono, Ph.D. Dissertation, Okayama University of Science (1991)
- [4] J. D. Scargle, Astro. Phys. J. 263, 835 (1982)
- [5] J. Orear, A. H. Rosenfeld, and R. A. Schluter, *Nuclear Physics, A Course Given by E. Fermi at Univ. of Chicago* (Univ. of Chicago Press, 1950)
- [6] L. Landau, *Lectures on Nuclear Theory* (New York Consultants Bureau, 1958)
- [7] K. Kinoshita, et al., Z. Phys. C8, 205 (1981)
- [8] K. Rubiki, Nuovo Cimento 28, 1437 (1963)
- [9] D. Abraham, et al., Phys. Rev. 159, 1110 (1967)
- [10] D. H. Perkins, *Introduction to High Energy Physics* (Addison-Wesley, 1987)
- [11] D. Griffiths, *Introduction to Elementary Particles* (John Wiley & Sons, 1987)
- [12] O. Miyamura, *Quark Matter* (Kyoritsu, 1985)
- [13] M. Guidry, *Gauge Field Theories* (John Wiley & Sons, 1991)
- [14] A. De Rujula, et al., Phys. Rev. D12, 147 (1975)
- [15] F. E. Close, *An Introduction to Quarks and Partons* (London Academic, 1979).
- [16] D. Lurie, *Particles and Fields* (John Wiley & Sons, 1968)
- [17] Y. Nambu and J-Lasinio, Phys. Rev. 122, 345(1961)
- [18] M. Johnson, Private Communication (2001)
- [19] G. Boyd, et al., Phys. Lett. B349, 170 (1995)
- [20] T. Hatsuda, Nucl. Phys. A544, 27c (1992)
- [21] S. Nagamiya, Nucl. Phys. A488, 3c (1988)
- [22] B. Muller, Rep. Prog. Phys. 58, 661 (1995) and References Therein
- [23] E802 Collaboration, Phys. Lett. B197, 285 (1987); Z. Phys. C38, 35 (1988)
- [24] WA80 Collaboration, Phys. Lett. B202, 596 (1988)

- [25] M. J. Tannenbaum, Nucl. Phys. A488, 555c (1988)
- [26] WA80 Collaboration, Phys. Lett. B199, 297 (1987)
- [27] E814 Collaboration, Z. Phys. C38, 45 (1988)
- [28] P. Braun-Munzinger, Nucl. Phys. A544, 137c (1992)
- [29] J. Stachel, et al., Phys. Lett. B216, 1 (1990)
- [30] NA35 Collaboration, Phys. Lett. B184, 285 (1987)
- [31] H. Sorge, Phys. Rev. C52, 3291 (1995)
- [32] J. D. Bjorken, Phys. Rev. D27, 140 (1983)
- [33] W.A. Zajc, Phys. Rev. D35, 3396 (1987)
- [34] S. Nagamiya, Nucl. Phys. A400, 399 (1983)
- [35] F. B. Yano and S. E. Koonin, Phys. Lett. 78B, 556 (1978)
- [36] P. Koch, B. Muller, and J. Rafelski, Phys. Rep. 142, 167 (1986)
- [37] T. Matsui and H. Satz, Phys. Lett. B178, 416 (1986)
- [38] U. Heinz and M. Jacob, New State of Matter Created at CERN (<http://pressold.web.cern.ch/PressOld/Releases00/PR01.00EQuarkGluonMatter.html>)
- [39] A. Takeda, *Soryushi* (Shokabo, 1986)
- [40] T. Ericson and W. Weise, *Pions and Nuclei* (Oxford University Press, 1988)
- [41] V. Koch, LBL Preprint, LBL-38000 (1995)
- [42] M. Gell-man and M. Levy, Nuovo Cimento 16, 53 (1960)
- [43] V. Koch, et al., LBL Preprint, LBL-40176 (1997)
- [44] S. Gavin, Nucl. Phys. A590, 163c (1995)
- [45] K. Rajagopal and F. Wilczek, Nucl. Phys. B404, 577 (1993)
- [46] S. Gavin, A. Goksch, and R.D. Pisarski, Phys. Rev. Lett. 72, 2143 (1994)
- [47] S. Gavin and B. Müller, Phys. Lett. B329, 486 (1994)
- [48] M. Asakawa, Z. Huang, and X. N. Wang, Phys. Rev. Lett. 74, 3126 (1995)
- [49] D. Boyanovsky, H. J. de Vega, and R. Holman, Phys. Rev. D51, 734 (1995)
- [50] F. Cooper, Y. Kluger, E. Mottola, and J. P. Paz, Phys. Rev. D51, 2377 (1995)
- [51] Y. Kluger, F. Cooper, and E. Mottola, Phys. Rev. C54, 3298 (1996)
- [52] J. Randrup, Phys. Rev. Lett. 77, 1226 (1996)
- [53] A. A. Anselm and M.G. Ryskin, Phys. Lett. B266, 482 (1991)
- [54] J. P. Blaizot and A. Krzywcki, Phys. Rev. D46, 246 (1992)
- [55] J. D. Bjorken, Acta Phys. Pol. B23, 561 (1992)
- [56] Z. Huang and X. N. Wang, Phys. Rev. D49, 4335 (1994)

- [57] R. D. Amado and Y. Lu, *Phys. Rev. D* **54**, 7075 (1996)
- [58] J. Randrup, *Nucl. Phys. A* **616**, 531 (1997)
- [59] Z. Huang, I. Sarcevic, R. Thews, and X. N. Wang, *Phys. Rev. D* **54**, 750 (1996)
- [60] J. Randrup and R. Thews, *Phys. Rev. D* **97**, 4392 (1997)
- [61] Chakaltaya-Pamir Collaboration, Tokyo University Preprint, ICRR-Report-258-91-27 (1991) and References Therein
- [62] J. D. Bjorken, et al., SLAC Preprint, SLAC-PUB-6109 (1993)
- [63] S. L. Adler, *Phys. Rev.* **177**, 2426 (1969)
- [64] J. S. Bell and R. Jackiw, *Nuovo Cimento A* **60**, 47 (1969)
- [65] H. Minakata and B. Müller, *Phys. Lett. B* **377**, 135 (1996)
- [66] M. Asakawa, et al., *Phys. Rev. C* **65**, 057901 (2002)
- [67] Y. Takahashi, et al., The University of Alabama in Huntsville, Research Proposal No. 90-188 (1990)
- [68] A. Iyono, Private Communication (1993)
- [69] G. Romano, et al., CERN Proposal CERN-SPSC-89-1; SPSC-P-243 (1989)
- [70] T. Virgili, Private Communication (1993)
- [71] Y. Takahashi, et al., CERN Proposal CERN-SPSLC-93-18; SPSLC-P-176 (1993)
- [72] NA34 Collaboration, *Z. Phys. C* **46**, 361 (1990)
- [73] Y. Takahashi, Private Communication (1992)
- [74] W. Press, S. Teukolsky, W. Vetterling, and B. Flannery, *Numerical Recipes in C* (Cambridge University Press, 1992)